Extraterrestrial Oceanography of Titan's Northern Seas from *Cassini* VIMS Sun Glitter Observations

Presented in Partial Fulfillment of
the Requirements for the Degree of

Master of Science

with a Major in

Physics

in the

College of Graduate Studies

University of Idaho

by

Michael Francis Heslar

Major Professor
Jason Barnes, Ph.D.

Committee
Matthew Hedman, Ph.D.
Timothy Bartholomaus, Ph.D.

Department Administrator
John Hiller, Ph.D.

December 2022

Abstract

In this thesis, I investigate the occurrence of sun glitter and waves on the sea surfaces of Titan's northern seas, Kraken Mare and Punga Mare. These studies of various sun glitter features help to uncover unique liquid bodies, such as liquid-filled channels, better understand the dynamics behind the air-sea-land interactions during the northern summer. Some of these interactions include wind-generated capillary waves, tidal currents, and wave shoaling.

In Chapter 1, I introduce the physics of sunglint and sun glitter observations in a terrestrial context and elaborate on the spacecraft geometry that necessitates a sun glitter observation on Titan. In addition, I provide an overview of prior specular observations from the seas on Titan and the geographical context for Titan's seas.

In Chapter 2, I present *Cassini* VIMS observations of sun glitter – wave-induced reflections from a liquid surface offset from a specular point – on Kraken Mare. Sun glitter reveals rough sea surfaces around Kraken Mare, namely the coasts and narrow straits. The sun glitter observations indicate wave activity driven by the winds and tidal currents in Kraken Mare during northern summer. T104 *Cassini* VIMS observations show three sun glitter features in Bayta Fretum indicative of variegated wave fields. I cannot uniquely determine one source for the coastal Bayta waves, but I lean toward the interpretation of surface winds, because tidal currents should be too weak to generate capillary-gravity waves in Bayta Fretum. T105 and T110 observations reveal wave fields in the straits of Seldon Fretum, Lulworth Sinus, and Tunu Sinus that likely originate from the constriction of tidal currents. Coastlines of Bermoothes and Hufaidh Insulae adjoin rough sea surfaces, suggesting a complex interplay of wind-roughened seas and localized tidal currents. Bermoothes and Hufaidh Insulae may share characteristics of either the Torres Strait off Australia or the Åland region of Finland, summarized as an island-dense strait with shallow bathymetry that hosts complex surface circulation patterns. Hufaidh Insulae could host seafloor bedforms formed by tidal currents with an abundant sediment supply, similar to the Torres Strait. The coastlines of Hufaidh and Bermoothes Insulae

likely host ria or flooded coastal inlets, suggesting the Insulae may be local peaks of primordial crust isolated by an episode of sea-level rise or tectonic uplift.

In Chapter 3, I present new evidence for active coastal and oceanic features in Titan's Punga Mare observed in a high-phase *Cassini* VIMS observation of sunglint from the T110 flyby. I observe sunglint in a river, Apanohuaya Flumen, resulting from differing pixel contributions of land adjacent to the channel and implying smooth liquid surfaces. Along the eastern coastline, I identify a 5-μm-bright margin. A possible explanation for this brightening may include a coastal margin of rough seas. I find evidence of variegated sea surface roughness in Fundy Sinus and isolated sun glitter near Hawaiki Insulae that suggests seasonal interactions between surface winds and topography. RADAR observations of debouches (where rivers meet bays) within Punga Mare overlap several bright 5 μm pixels that indicate rough liquid surfaces. We postulate that a change in liquid flow regimes, possibly occurring as surface streamflow, or bubble outburst events may be responsible for surface roughness near these debouches. These observations imply air-sea-land interactions and hydrological activity are present in Titan's sea district during the northern summer.

In Chapter 4, I summarize the implications of the various sun glitter observations on Titan oceanography.

Acknowledgements

I started my undergraduate degree with no real certainty for my future beyond wanting to study the universe. Once I ended up working at a research internship in a Titan simulation chamber at the University of Arkansas, I was exposed to the amazingly Earth-like world of Titan. I became intrigued with further studying Titan after that internship. And after extensive graduate school applications, I must first acknowledge my immense gratitude for my advisor Dr. Jason Barnes to offer the opportunity to continue research on Titan. I appreciate how he allowed me the freedom to explore the plethora of imagery from the Cassini mission and decide my own research focus. Jason provided me with the necessary assistance to complete my first independent scientific investigation, write up the publication over many red-ink reviews, and successfully publish the results. From there, I was able to take charge on several more projects studying various aspects of Titan and really live my dream working as a planetary scientist. I will forever be grateful for his time and patience he gave to be a great mentor. I hope to apply my new scientific skills in a new research field for my future career, whether on Titan or another planet.

I extend my gratitude towards my dissertation committee members, Dr. Matthew Hedman and Dr. Timothy Bartholomaus, for offering their time and expertise. I want to thank Dr. Matthew Hedman for his assistance and open-door policy whenever I ran into education or technical issues during my time in the department.

Acknowledgements to my fellow lab and class mates, Steven Kreyche, Daniel Coulter, Sanjoy Saha, Rajani Dhingra, Himanshi Sharma, Will Miller, and Ross who helped me through the struggles of graduate classes and made the lab environment challenging and interesting, at least before the unsuspecting covid-19 pandemic shut down the world.

Finally, I acknowledge the support of the University of Idaho Department of Physics and NASA's Cassini Data Analysis and Participating Scientists (CDAPS) Program for their financial support to pursue my graduate studies.

Dedication

To my parents, Thomas Heslar and Lisa Bray, who graciously helped bring and raise me into this world

To my aunt and uncle, Terri Yoshihata and Michael Heslar, for their unwavering support of my dreams

To my grandfather, William Heslar, for helping incite my early curiosity for science

Statement of Collaboration

Two chapters from my thesis have been published elsewhere:

Chapter 2 has been previously published:

> Significant work from this chapter has been published in the *Planetary Science Journal* upon writing this chapter. The current citation is "Heslar M.F., Barnes J.W., Soderblom J.M., Seignovert B., Dhingra R.D., and Sotin C. 2020. Tidal Currents Detected in Kraken Mare Straits from Cassini VIMS Sun Glitter Observations. *Planetary Science Journal* 1:35."

I specifically conducted most of the data collection (VIMS image cubes) and analysis, generation of most figures, and writing of the subsequent publication (listed in the footnote). My advisor, Dr. Jason Barnes, collaborated on discussions related to the interpretation of the data analysis and provided many suggestions for improvements with the writing of the manuscript. In addition, my fellow co-authors also provided peer review to improve the writing of the manuscript.

Chapter 3 has been undergoing the peer review process:

> Significant work from this chapter was going through the peer review process for publication in the Planetary Science Journal when writing this chapter. Current citation is Heslar M.F. & Barnes J.W. 2022 *Planetary Science Journal*. (under review)

I performed the data collection, analysis, and possible physical interpretations of the sun glitter features discussed in this chapter. I generated all of the figures and wrote up the majority of the manuscript. My corresponding author and advisor, Dr. Jason Barnes, contributed significant advice on the investigations of possible interpretations for the features and recommendations on figure and writing improvements. Furthermore, Dr. Barnes provided significant help in understanding the background of the various concepts related to the science of sunglint, sun glitter, comparative planetology, and VIMS image cubes needed to analyze the datasets.

Table of Contents

List of Tables

List of Figures

CHAPTER 1

Introduction

1.1 Titan and its hydrocarbon seas

Titan is an intriguing planetary satellite orbiting Saturn that hosts a thick atmosphere of mostly nitrogen and methane at 94.2% and 5.6% respectively (Lorenz and Mitton, 2010). Looking at Titan with human eyes in Figure 1.1 reveals a thick veil of aerosols and tholins that shrouds the surface. Titan has a surface pressure of 1.5 bars that is only 50% more than Earth (Lindal *et al.*, 1983), but has a very different surface temperature regime from Earth ranging between 89 and 95 K (Flasar *et al.*, 2005). The eccentricity of 0.028 for Titan's orbit around Saturn **?** and Saturn's axial tilt of 26.7° allows for seasonal variations in insolation that drives a dynamic atmosphere with Hadley circulation patterns on Titan (Mitchell and Lora, 2016).

The second main atmospheric constituent of methane at Titan's temperature and surface pressure conditions occur close to its triple point, where it can transition between the gas, liquid, and solid states of matter (Roe, 2012). As a result, liquid methane can remain stable on the surface while methane vapor exists in the lower atmosphere, mainly the troposphere (Roe, 2012). This situation is analogous with water cycle and weather patterns in the troposphere of Earth. In a similar manner on Titan, the "methanological" cycle on Titan that includes methane and ethane clouds, rain, surface liquid bodies, and even subsurface liquid reservoirs (Lunine and Atreya, 2008; Hayes, 2016). Further details are shown in a post-Cassini summary of the methanological cycle in Figure 1.2. Numerous surface features on Titan further suggest the influence of liquids, such as evaporite deposits (Barnes *et al.*, 2011a), channeled terrains (Malaska *et al.*, 2020), and hydrocarbon liquid bodies (Mitri *et al.*, 2007). In addition, the variations in surface conditions facilitate a dynamic air-sea-land environment with seasonal surface winds (Hayes *et al.*, 2013), daily tides and currents, methane evaporation and precipitation (Barnes *et al.*, 2013a; Chatain *et al.*, 2022), and fluvial and coastal activity (Hayes, 2016).

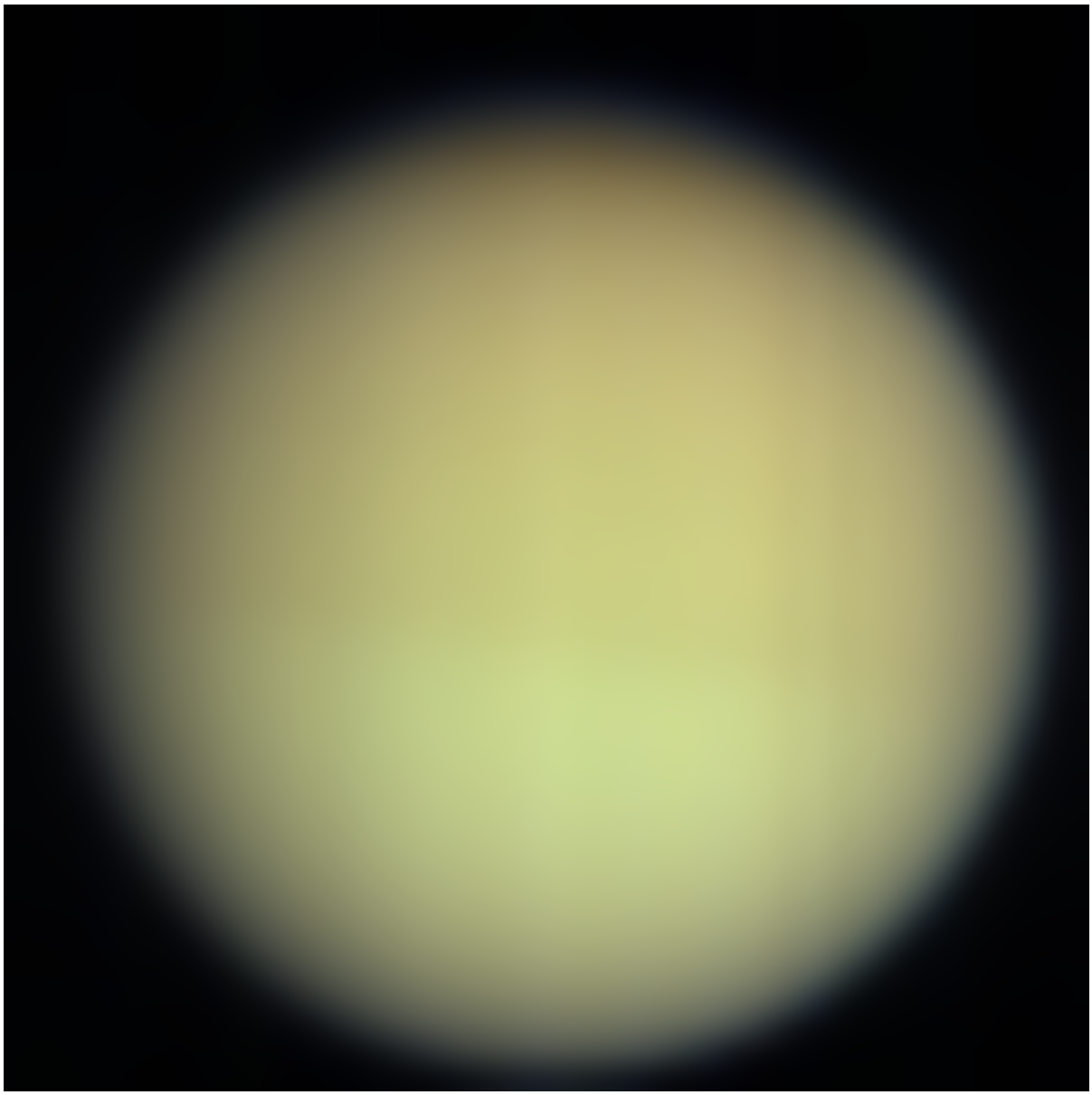

FIGURE 1.1: A visible color image of Titan by the Visual and Infrared Mapping Spectrometer - Visible (VIMS-V) instrument shows a smooth orange color caused by haze scattering and atmospheric absorption (primarily methane). The surface is hidden at visible wavelengths. North is upwards in the image.

The polar regions of Titan, in particular, host a complex array of liquid bodies that are familiar on Earth, namely rivers (Flumen/Flumina), bays (Sinus), straits (Fretum/Freta), islands (Insula/Insulae), lakes (Lacus), and seas (Mare/Maria) within the "Lakes" map unit in Figure 1.3. The sizes of Titan's methane seas are quite comparable to seas or large lakes on Earth (Hayes, 2016). The largest methane sea Kraken Mare is approximately 500,000 km^2, slightly larger than the Red Sea (438,000 km^2). Meanwhile, the smallest methane sea Punga Mare is similar in size to Lake Michigan (58,030 km^2) at approximately 61,400 km^2. Unsurprisingly, the majority of surface liquids reside in the hydrocarbon seas of the north polar latitudes (Mitri *et al.*, 2007; Stofan *et al.*, 2007). Air-sea-land interactions similar to those of Earth, such as wind-waves and surface currents, were anticipated in the surrounding areas of these (theoretically before 2007) vast hydrocarbon seas (Ghafoor *et al.*, 2000; Lorenz, 2003; Lorenz *et al.*, 2003; Ori *et al.*, 1998). With the arrival of *Cassini* to the Saturn system, these interactions were observable as possible waves or other anomalies on the large hydrocarbon sea surfaces.

Initial surveys of specular reflections on Ontario Lacus, Jingpo Lacus, and Ligeia Mare turned out to be very smooth and lacked any signature of waves (Barnes *et al.*, 2011b; Wye *et al.*, 2009; Zebker *et al.*, 2014). A T59 specular reflection observed over Kraken Mare produced an inconclusive light curve, but wind or wave activity was postulated (Barnes *et al.*, 2011b). In the late northern spring, Barnes *et al.* (2014) found several isolated bright pixels on Punga Mare during the T85 flyby (northern spring), providing the first definitive evidence of extraterrestrial waves. Soon after, the detection of RADAR-bright "magic islands" in Ligeia Mare were also theorized to be surface waves (Hofgartner *et al.*, 2014, 2016). Recent findings suggest Kraken Mare sea surface roughness constraints at 6-10 mm from RADAR altimeter measurements (Grima *et al.*, 2017) and $<$3.6 cm from isolated bistatic RADAR observations (Marouf *et al.*, 2016). Many theoretical circulation models have also supported different seasonal mechanisms for possible large-scale wave generation in the northern summer, including wind circulation (Tokano and Lorenz, 2015), sea breezes (Chatain *et al.*,

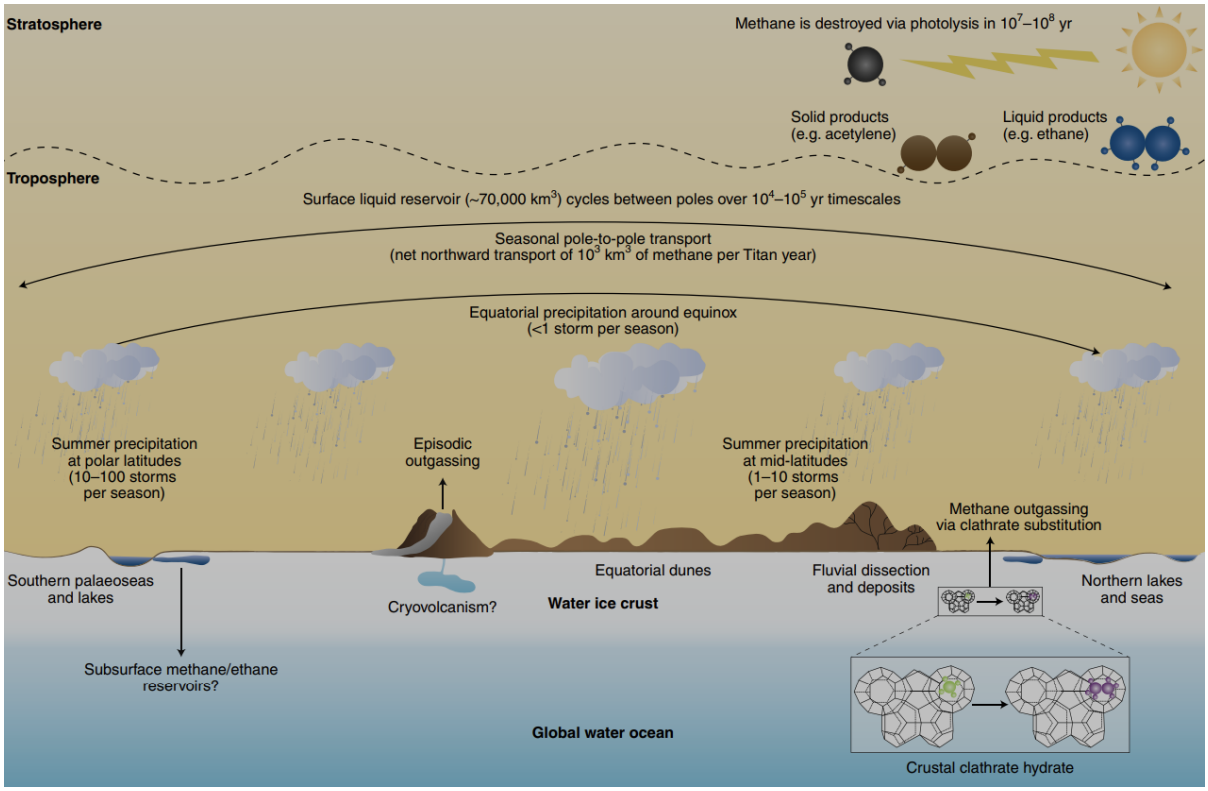

FIGURE 1.2: The methanological cycle of Titan at different latitudes, going left to right for the south to north poles respectively. Source: Figure 4 from Hayes *et al.* (2018)

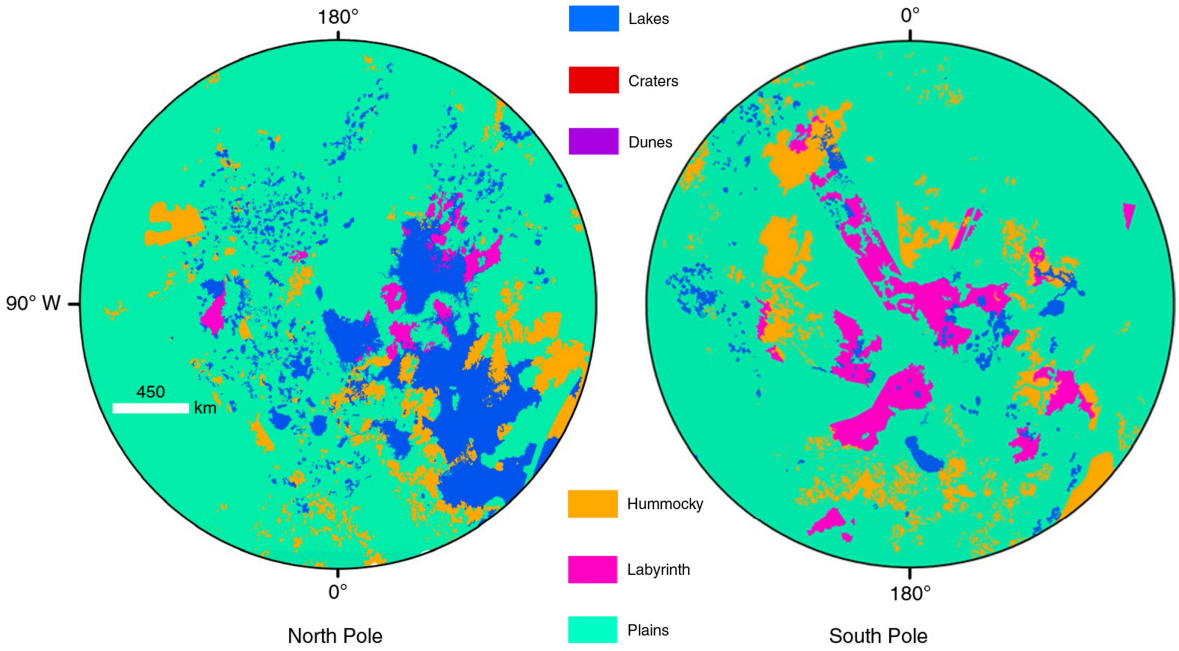

FIGURE 1.3: A diversity of terrain types and liquid bodies, such as lakes and seas, are seen in the north and south polar projections of a Titan geomorphological classification map derived from *Cassini* imagery datasets. Source: modified Figure 2 from Lopes *et al*. (2019b).

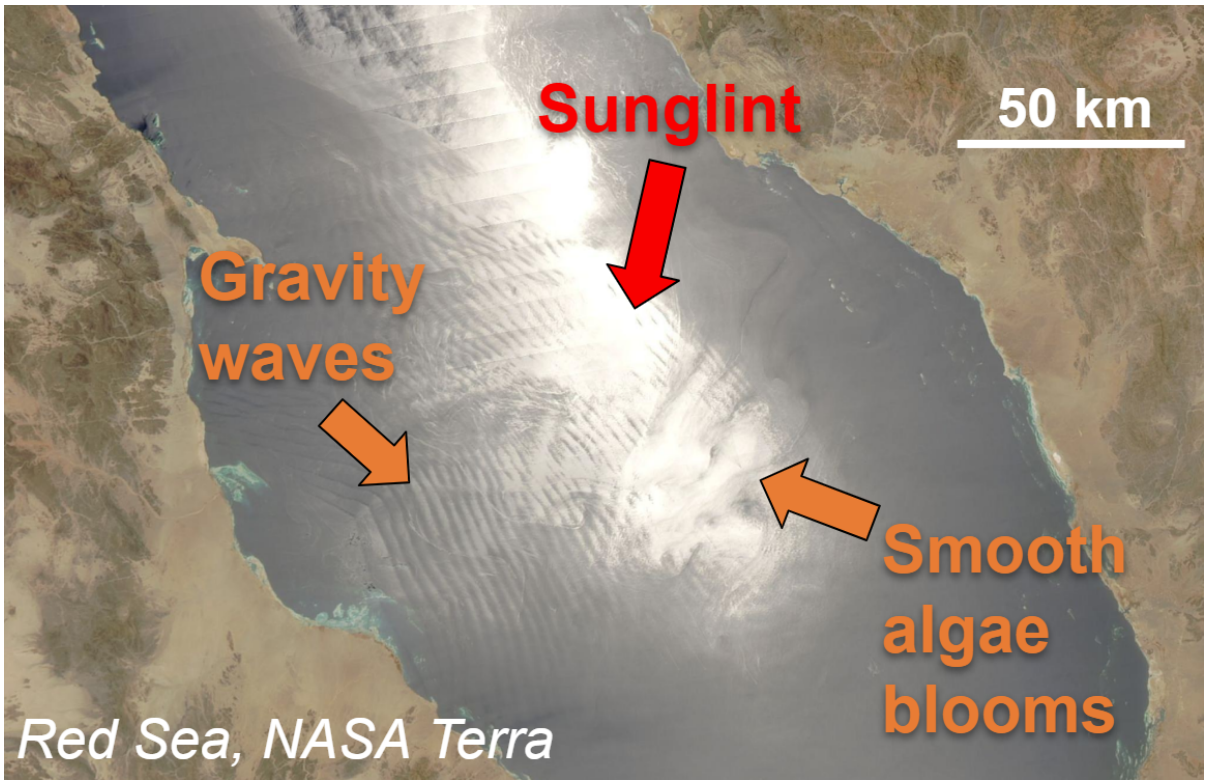

FIGURE 1.4: A true color NASA Aqua MODIS image of sunglint and sun glitter features on the Red Sea taken on 29 July 2013. A blinding glare of sunglint saturates the middle of the image, while the surrounding area of sun glitter reveals rough atmospheric gravity waves overlapped by algae blooms that dampen surface waves.

2022), and solar heating (Tokano and Lorenz, 2016), even if they may occur on an ephemeral basis.

1.2 PHYSICS OF SUN GLITTER

[1]

On Earth, oceanographers often observe surface waves over the seas and oceans from remote sensing (Bréon and Henriot, 2006). Surface waves represent macroscopic sea surface roughness that cause a broad, specular surface reflectance phase function

[1]Significant portions of this section are taken from the following references:
Heslar *et al*. (2020): "Heslar M.F., Barnes J.W., Soderblom J.M., Seignovert B., Dhingra R.D., and Sotin C. 2020. Tidal Currents Detected in Kraken Mare Straits from Cassini VIMS Sun Glitter Observations. *Planetary Science Journal* 1:35."
Heslar M.F. & Barnes J.W. 2022 *Planetary Science Journal*. (under review)

known as sun glitter. Sun glitter imagery can reveal important details about the local environmental conditions on the surface, such as wind speeds (Bréon and Henriot, 2006) and ocean currents (Kudryavtsev *et al.*, 2017). I show an example of intriguing surface features, such as atmospheric gravity waves that periodically bounce up and down on the sea surface (Nappo, 2013), captured in a typical satellite image with sunglint on the Red Sea in Figure 1.4 to highlight the real potential of sunglint imagery to uncover oceanographic phenomena from orbit. Oceanographers can also infer information about oceanographic processes beneath the sea, such as the stratification of water masses (Jackson, 2007). Similar sun glitter observations could yield useful insights in the oceanographic processes on Titan, which may rival the complexity in Earth's oceans (Lorenz, 2013).

Liquid bodies act like mirrors when liquids have sea surface heights smaller than the observing wavelength of the spectrometer (Barnes *et al.*, 2011b). Satellites see blinding specular reflections of the Sun when in the appropriate observational geometry. As Figure 1.5 illustrates, a satellite observes sun glitter as bright spots with enhanced reflectivity in the vicinity of the specular point.

Sun glitter often occurs in isolated regions, separate from the specular reflection, where the sea surface is rougher (i.e. larger sea surface height anomalies) and some facets tilt toward the observer (*Cassini*). I quantify the sea surface roughness by the specular deviation angle (θ in Figure 1.5), which describes the angle at which the liquid surface needs to be tilted toward an observer to achieve a specular reflection.

For Titan, the Visual and Infrared Mapping Spectrometer (VIMS) (Brown *et al.*, 2004) observes solar specular reflections as bright or possibly saturated pixels in the atmospheric windows used for the color image of Figure 1.6. In particular, the 5 μm window shows a preferential enhancement in brightness (Stephan *et al.*, 2010; Sotin *et al.*, 2012), indicating the reflector is at the surface. The specular reflection is accompanied by an aureole in the surrounding annulus of pixels (Stephan *et al.*, 2010; Barnes *et al.*, 2013b, 2014). I denote this region of intense reflectance and forward-scattering (Tomasko *et al.*, 2008) with specular deviation angles less than two degrees as the "specular zone" in this paper. I also define a "sun glitter zone"

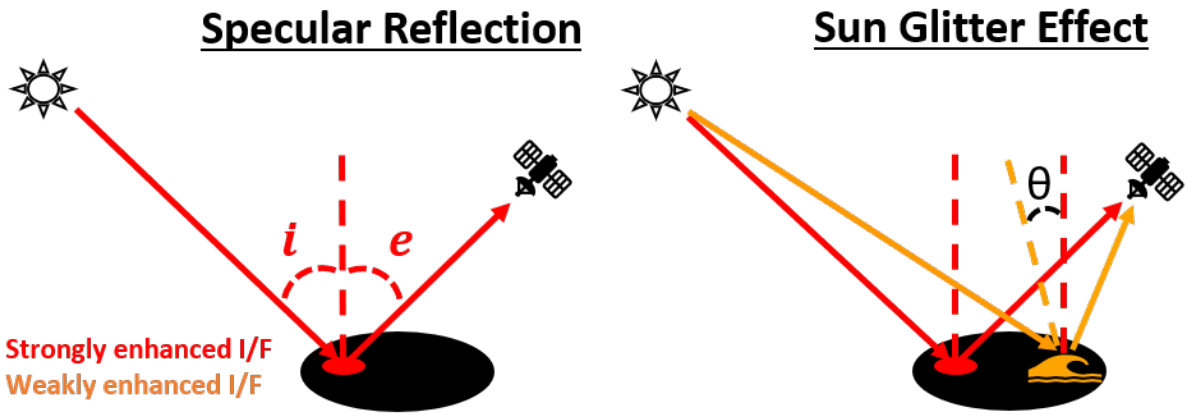

FIGURE 1.5: This cartoon illustrates the observation geometry of a specular reflection (sunlight directly reflected off a planetary surface) and sun glitter (waves tilting the liquid surface toward an observer, like *Cassini* VIMS) off a dark Titan sea surface in the left and right diagrams respectively. The red and orange dashed lines indicate the local surface normals for flat and rough liquid surfaces. The incidence and emission angles are i and e, which are in the same plane and equal to each other for both cases. Sun glitter retains a specular geometry but instead tilts the surface normal by θ, known as the specular deviation angle. Red and orange colors represent strongly enhanced radiance from a flat sea surface compared to weakly enhanced radiance from a rough sea surface. I/F is the ratio of observed to incident flux measured by the *Cassini* Visual and Infrared Mapping Spectrometer (VIMS).

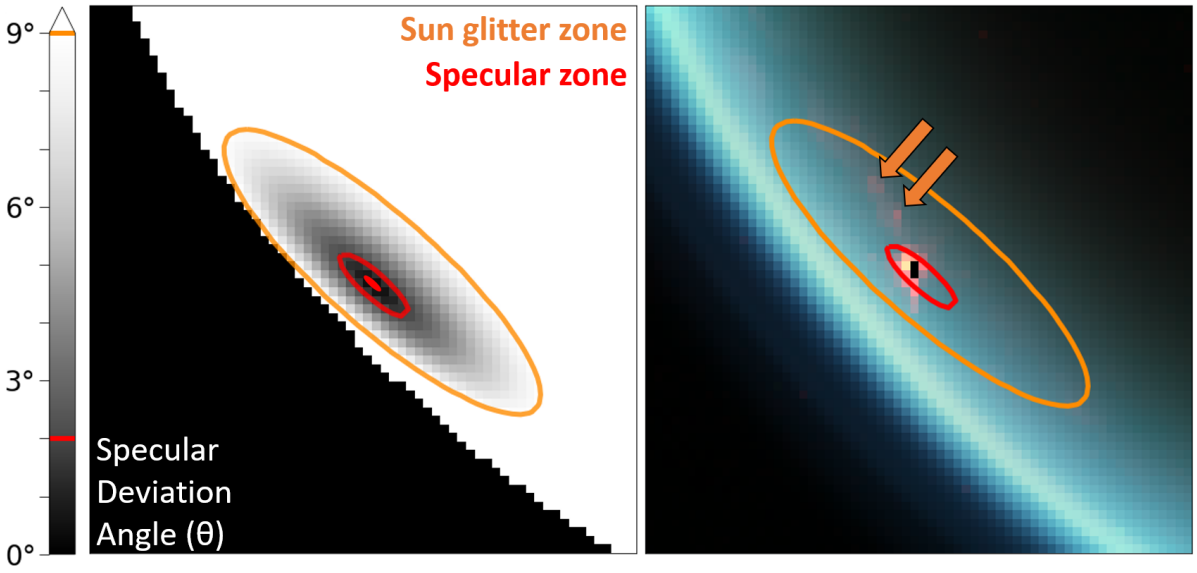

FIGURE 1.6: The left image shows a modeled specular deviation angle (θ) map for the first-documented VIMS cube, CM_1721848119_1, with sun glitter modified from Barnes *et al*. (2014). The right image shows the corresponding cube with a wet-sidewalk color scheme (RGB: 5.0, 2.03, 2.79 μm) (Dhingra *et al*., 2019). The red and orange ellipses represent the theoretical specular and sun glitter zones (θ = 2 and 9° respectively). The orange arrows identify the brightened pixels appearing in the sun glitter zone, where VIMS is most sensitive to sun glitter. In the left image, a filled red ellipse indicates the theoretical specular point, which is observed as saturation in the two black pixels of the right image.

as an annulus around the specular zone where sun glitter can be easily detected as regions of weakly enhanced reflectance relative to the darker liquid surface, shown in Figure 1.6. The sun glitter zone is likely confined to a specular deviation angle of ~9-10° due to the similar steepness ratio (wave height to wavelength) for breaking waves in liquid methane and water (Craik *et al*., 2004; Hayes *et al*., 2013).

Even liquid bodies smaller than Punga Mare, such as Ontario Lacus (16,200 km^2), showed evidence of wave-modified coastal morphology (Wall *et al*., 2010) and wetted shorelines (Barnes *et al*., 2009). Furthermore, ocean circulation models of Titan's seas suggested that density-driven, precipitation-driven, and insolation-driven circulations develop during the summer (Tokano and Lorenz, 2015, 2016). Studies on the marine environments of Punga Mare remain limited, but are suggestive of mostly flooded coastlines (Mastrogiuseppe *et al*., 2018). During the T110 flyby, *Cassini* VIMS

recorded a single specular observation of Punga Mare, hereafter called the "T110 observation".

This master's thesis investigates the occurrence of sun glitter and waves on the sea surfaces of Titan's northern seas in VIMS cube infrared images during the summer. chapter 2 describes moderate-sampling (∼17-21 km) sun glitter observations in large areas of Kraken Mare as observed by specific near-infrared (NIR) atmospheric windows of Titan's atmosphere during the T104, T105, and T110 Titan flybys. This section discusses the implications of the sun glitter in constricted straits and along coastlines of the maria to probe oceanic processes, including tides and wind activity. chapter 3 describes the T110 observation metadata and the geographic context of Punga Mare and discusses the details of each specular feature and its possible causes with hydrological and geographical context. chapter 4 elaborates on the implications of these sun glitter observations on the overall understanding of oceanography on Titan.

CHAPTER 2

Kraken Mare Sun Glitter Observations[2]

When I first arrived to the Barnes research group, I was not sure what to initially pursue for a research project. So I had started perusing the available *Cassini* VIMS cube imagery to motivate some research ideas. I remembered reading my advisor's publication that announced the discovery of waves on the Titan's sea surfaces and kept coming across similar wave features in VIMS images of the later Titan flybys. From there, I compiled all of these wave observations, which are known as sun glitter in oceanography, in VIMS images taken at select infrared wavelengths where methane windows allow the observation of Titan's surface. In collaboration with my advisor and fellow Titan researchers Benoît Seignovert, Rajani Dhingra, Jason Soderblom, and Christophe Sotin, we published these results on the sun glitter observations in the *Planetary Science Journal*. These results included the confirmation of multiple tidal currents predicted by Titan tidal models and further evidence for wind capillary waves on Kraken Mare.

2.1 MODERATE-SAMPLING SUN GLITTER OBSERVATIONS

I focus our search for sun glitter in the later Titan flybys (after T100) that cover the northern spring and summer seasons with anticipated increases in capillary-gravity wave activity (Hayes *et al.*, 2013, Lorenz and Hayes, 2012). The northern spring and summer also offered the best chances to observe sun glitter with the constant daytime over the maria. I include some VIMS observation at coarse sampling ($\geq$10 km/pixel) with bright specular reflections from the T104 and T105 flybys in Table 3.1. The T104 and T105 flybys were accompanied with fine-sampling sun glitter observations ($<$10 km/pixel) over the same areas of Bayta and Seldon Freta.

[2]Originally published in Heslar *et al.* (2020):
"Heslar M.F., Barnes J.W., Soderblom J.M., Seignovert B., Dhingra R.D., and Sotin C. 2020. Tidal Currents Detected in Kraken Mare Straits from Cassini VIMS Sun Glitter Observations. *Planetary Science Journal* 1:35."

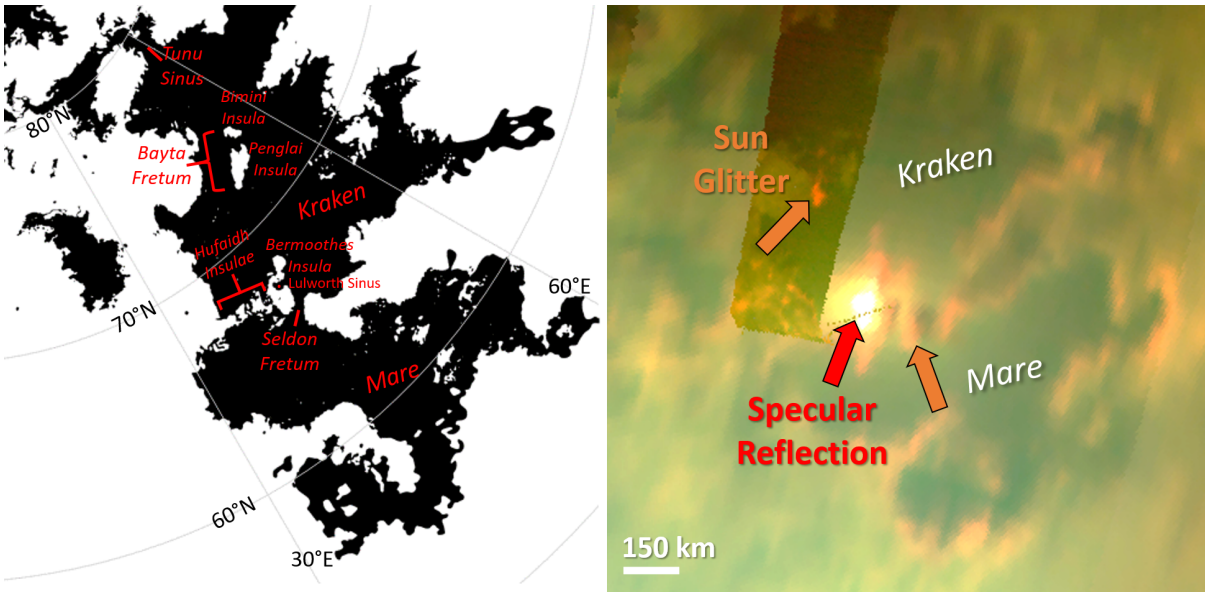

FIGURE 2.1: The left image shows a binary map of the Titan maria, derived from *Cassini* Imaging Science Subsystem (ISS) and RADAR data, and named features relevant for this publication. The right image shows the *Cassini* VIMS north polar map from the T104 flyby cropped onto Kraken Mare in the wet-sidewalk color scheme of Figure 1.6. Liquid surface features, specifically the specular reflection and sun glitter (red and orange arrows), appear as anomalously bright, uniform spots in the narrow straits or Freta of Kraken Mare.

In Figure 2.1, I showcase a color mosaic of several VIMS observations of the largest sea of Titan, Kraken Mare, collected from the T104 flyby on 2014 August 21. I display the data using a wet-sidewalk RGB color scheme with the three most transparent atmospheric windows of Titan: 5.0, 2.03, and 2.79 μm (Dhingra *et al.*, 2019). The left binary map in Figure 2.1 shows the relevant features that I discuss in this paper. Close flyby distances (≤50,000 km) to Titan allow us to observe details (≤25 km/pixel) of the surface and tropospheric features in the Titan sea district. The notable bright feature of the T104 mosaic in Figure 2.1 is a specular reflection and associated aureole caused by forward-scatter from haze (Barnes *et al.*, 2013b), which is located north of Hufaidh Insulae. The regions that appear bright pink in this color scheme (orange arrows in Figure 2.1) are areas of sun glitter because they are located away from the specular point and on known liquid surfaces.

I overlaid polar-projected VIMS observations averaged over the 5 μm window onto a global ISS map of Titan (Karkoschka *et al.*, 2017) to put the specular reflection

TABLE 2.1: Details on select VIMS observations with sun glitter for the T104, T105, T106, and T110 flybys. Each cube name starts with "CM_". SC Alt. is shorthand for spacecraft altitude. I denote the relative quality of the VIMS observation as "Fine" if its mean spatial sampling is less than 10 km/pixel. f represents true anomaly in degrees.

Flyby	Cube	Image mid-time	Sampling	Phase	Incidence	Emission	SC Alt.	f	Sampling
	*CM_*	*Date, Time [UTC]*	*[km/pixel]*	[°]	[°]	[°]	*[km]*	[°]	Quality
T104	1787311929_1	2014-08-21, 10:50:46	24	103	24-85	17-89	44,667	249	Coarse
T104	1787310233_1	2014-08-21, 10:04:53	17	102	43-58	44-60	35,502	248	Coarse
T104	1787307197_1	2014-08-21, 09:20:28	10	99	58-77	24-51	19,114	247	Coarse
T104	1787306033_1	2014-08-21, 08:54:53	7	97	57-62	35-40	12,879	247	Fine
T105	1790066425_1	2014-09-22, 07:45:01	21	109-111	23-77	37-89	42,680	248	Coarse
T105	1790059135_1	2014-09-22, 05:39:57	2	86-90	50-55	31-41	4,055	246	Fine
T105	1790059235_1	2014-09-22, 05:43:45	3	89-97	48-56	34-49	4,506	246	Fine
T106	1792827131_1	2014-10-24, 06:38:12	36	120	34-79	40-88	77,873	250	Coarse
T110	1805210863_1	2015-03-16, 14:30:21	2	75-108	49-53	58-66	2,408	246	Fine
T110	1805212073_1	2015-03-16, 14:49:48	3	133-135	58-73	62-75	8,219	246	Fine

and sun glitter into a geographical context in Figure 2.2. The 5 μm window has the highest transmission (>90%), which allows for the most detailed surface studies of Titan (Sotin *et al.*, 2012). I use Delaunay triangulation to interpolate the VIMS observation into a polar projection and retain the details of the raw data (Le Mouélic *et al.*, 2019a). I isolate the sun glitter zone with specular deviation angles between 2 and 9 degrees. Observational conditions of sun glitter, including spacecraft altitude (Soderblom *et al.*, 2012), airmass (Le Mouélic *et al.*, 2019a), and the specular deviation angle (Cox and Munk, 1954), vary for each Titan flyby and are corrected for an accurate comparison in Figure 2.2. I remove false positives (i.e. cosmic ray pixels) with a 3×3 low-pass filter if the pixels are only bright in a few neighboring spectral channels.

In the moderate-sampling 5 μm observations of Figure 2.2, the specular zone is confined to a small region of bright pixels that contains the specular point. In the sun glitter zone, I find several instances of sun glitter up to 350 km away during both T104 and T105 flybys. In particular, the sun glitter overlays the same locations in Kraken Mare, Bayta and Seldon Freta (narrow straits). Note that the large red feature in the T105 observation in Figure 2.2 is likely sun glitter, located to the east of Penglai Insula. The detection of sun glitter on two separate flybys may be indicative of consistently rough sea surfaces in the Freta of Kraken Mare. The presence of sun glitter is not surprising for coastal areas that are favorable for wave generation from turbulent surface currents (Dronkers, 2005, Lorenz, 2014), yet prior NIR and RADAR specular observations indicated smooth sea surfaces (Barnes *et al.*, 2011b, Hayes, 2016).

I note that the morphology of the observed sun glitter zone can provide insights to the overall sea state of Kraken Mare. Mainly, the T105 zone shows a larger areal extent and more elliptical profile. The Seldon sun glitter is brighter during the T104 flyby, while Bayta sun glitter shows similar I/F on both flybys. Overall, the sun glitter observations between the T104 and T105 flybys are suggestive of a variable, rough sea state in the north Kraken Mare region on two summer Titan days.

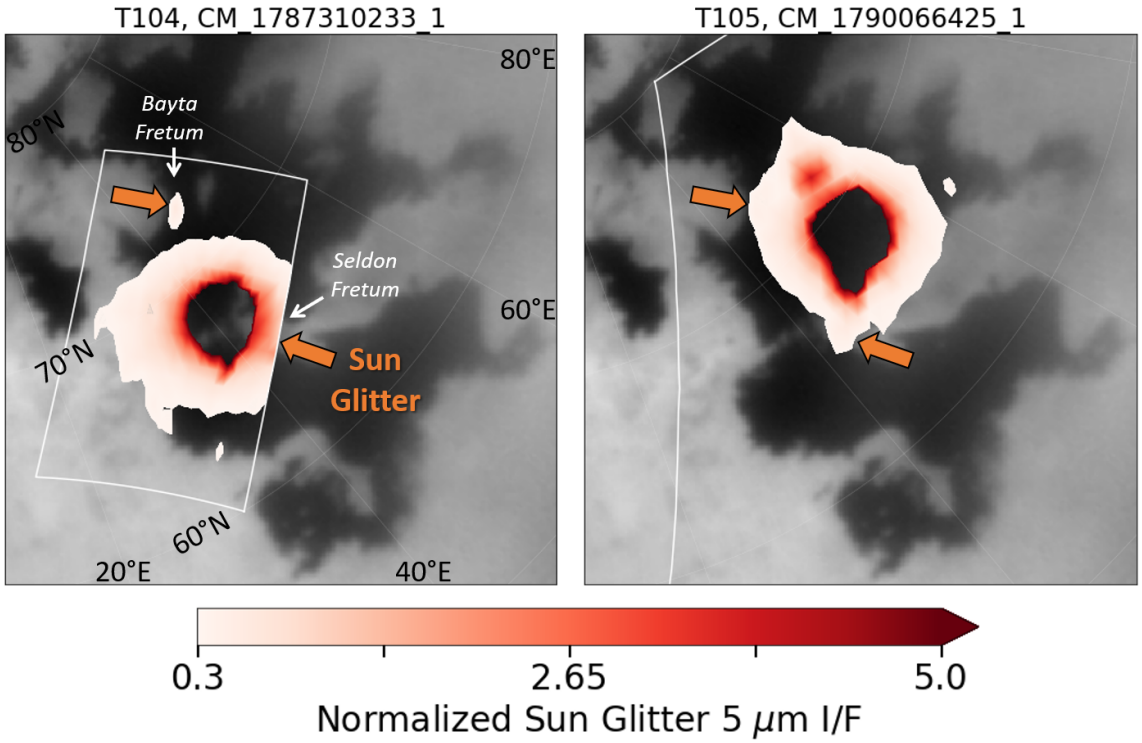

FIGURE 2.2: Probable regions of sun glitter are shown in the coarse-sampling VIMS cubes of Kraken Mare (∼17 and 21 km/pixel respectively) for T104 and T105 flybys, CM_1787310233_1 and CM_1790066425_1, in a normalized 5 μm polar projection. The 5 μm I/F is normalized by three factors: 1) the airmass used in Le Mouélic *et al.* (2019a), 2) a quadratic dependence of the specular deviation angle at the edge of the sun glitter zone (θ = 9°), and 3) a quadratic dependence of the spacecraft altitude at 44,000 km. The cubes are overlaid on an ISS basemap of Kraken Mare (Karkoschka *et al.*, 2017). The translucent grid lines represent lines of latitude and longitude. Sun glitter overlays Bayta and Seldon Freta (orange arrows) during both flybys, indicating persistent roughness in these regions.

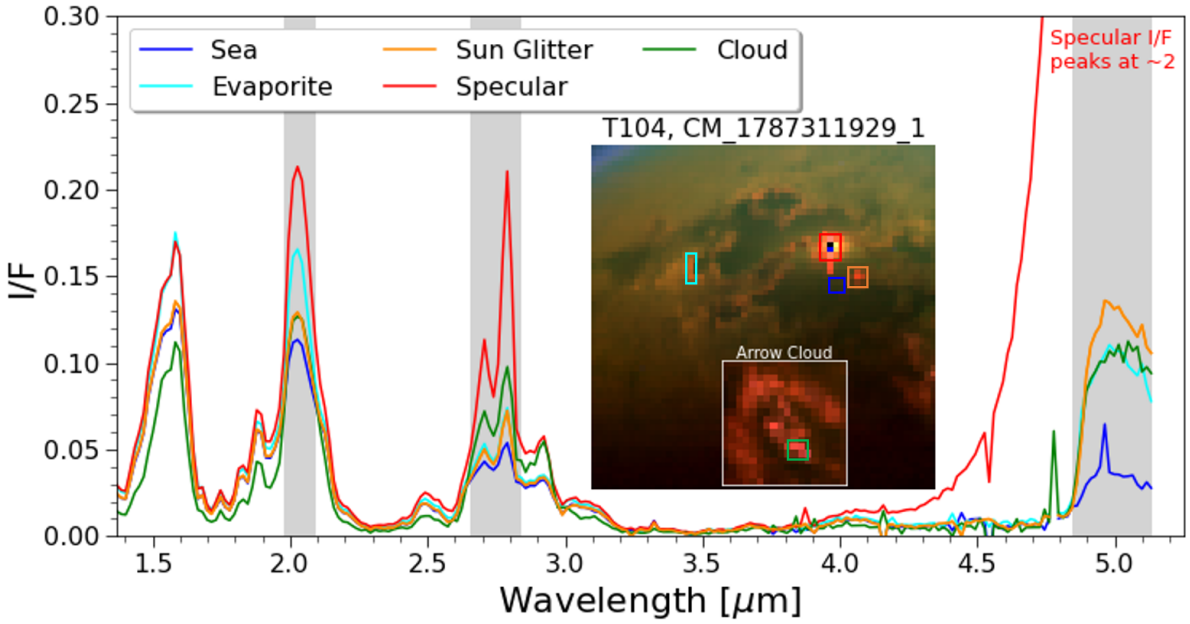

FIGURE 2.3: Near-IR spectra of surface and atmospheric features observed around Kraken Mare during the T104 flyby. Grey boxes indicate the transmission windows of Titan at 2.03, 2.75, and 5 μm. The inset plots show Kraken Mare from VIMS cube CM_1787311929_1 and the arrow cloud located north of Kraken Mare from cube CM_1787307197_1 with the same RGB color scheme as Figure 1.6. Spectral units are identified in the inset plot by boxes of the corresponding color. The spectra for evaporites and clouds show similar brightened I/F values for the 5 μm transmission window, while the hydrocarbon sea is the darkest surface feature. Evaporites are bright 5 μm deposits nestled along certain Kraken Mare coastlines. The brightest features are the non-saturated specular reflection and sun glitter observed in western Kraken Mare. The specular reflection pixel reaches a peak I/F of ~2.

2.2 SPECTRAL ANALYSIS

I derive the spectral information of various features using individual VIMS spectra in this section. In Figure 2.3, I compare the spectra of the notable surface features, namely the hydrocarbon sea, evaporite deposits, sun glitter, and a specular reflection, from T104 VIMS cube CM_1787311929_1 due to its large spatial coverage at moderate sampling (24 km/pixel). The main atmospheric feature, tropospheric clouds, was observed in the T104 VIMS cube CM_1787307197_1 with a notable arrowhead shape. The cloud spectrum in Figure 2.3 shows enhanced brightness in all methane transmission windows down to 2 μm with the characteristic bumps in the 2.12 μm wing and 2.9 μm window, which are common properties of high Titan clouds (Brown *et al.*,

2009, Griffith *et al.*, 2000, Rodriguez *et al.*, 2011, Turtle *et al.*, 2018). The sea spectrum shows that the hydrocarbon seas have the strongest near-IR absorption and appear rather uniform across Titan's surface as seen in the inset image in Figure 2.3.

The evaporite deposits are known to be bright at mainly 5 μm and have been documented along this coastal region of southeast Kraken Mare during many flybys (MacKenzie *et al.*, 2014, MacKenzie and Barnes, 2016). I note an increased 2 μm brightness of the evaporite spectrum in Figure 2.3. To our best knowledge, the surface phase function and composition of Titan evaporites remain unknown (MacKenzie and Barnes, 2016). Nonetheless, I identify evaporites as a fixed coastal feature of Kraken Mare.

The 5 μm saturated pixels covering known areas of Kraken Mare are a clear sign of a specular reflection at a close spacecraft altitude (Soderblom *et al.*, 2012). The brightest non-saturated pixel leaves no doubt of its specular nature as it goes off the chart in Figure 2.3. Also, there are reports of "bright ephemeral features" (BEFs) during north polar summer, possibly caused by wetted surfaces or fog (Dhingra *et al.*, 2019, Dhingra *et al.*, 2020). I show a T106 VIMS observation of a BEF in Figure 2.4 where there is potential sun glitter in Kraken Mare for direct comparison. I observe set of pink pixels near the specular reflection in Figure 2.4 but inside the sun glitter zone, which I attribute to the possible sun glitter. Conversely, I observe the large, documented wet-sidewalk feature (Dhingra *et al.*, 2020) at a larger specular deviation angle of 14° in Figure 2.4. A comparison of their spectra in Figure 2.4 shows the BEF is dimmer than the sun glitter in the transmission windows. Thus, I am reasonably confident that the BEF is distinct from sun glitter from the T106 observation. The distinguishing features of the BEF include a large areal coverage over land and Ligeia Mare and a location outside of the sun glitter zone that is not consistent with rough sea surfaces.

This just leaves the sun glitter spectrum seen as the second brightest feature at 5 μm in Figure 2.3. Previous sun glitter observations from the T85 flyby (Barnes *et al.*, 2014) likely only observed sun glitter at 5 μm due to strong forward-scattering at a high incidence angle of ∼73° (Soderblom *et al.*, 2012). Hence, the atmospheric

scattering exceeds the surface reflectance for the sun glitter pixels, making the sun glitter indiscernible at wavelengths shorter than 5 μm. However, there is no physical reason why *Cassini* VIMS cannot view sun glitter at shorter wavelengths. Figure 2.3 confirms that the T104 sun glitter spectrum is brighter than the sea spectrum in the 2.03 and 2.75 μm windows at an incidence angle of ∼55°.

2.3 FINE-SAMPLING SUN GLITTER OBSERVATIONS

I turn our attention to an analysis of fine-sampling (<10 km/pixel) observations of sun glitter in preferential areas of wave activity in the narrow straits (Freta) of Kraken Mare. I note that the relative location of the theoretical specular point becomes an issue of concern for fine-sampling observations. For moderate sampling (∼20 km/pixel), the theoretical specular point is generally confined to a single pixel for the observation time of the cube. While closer in to Titan, however, I need to consider how the illumination geometry may change over the observation time of a fine-sampling VIMS cube as *Cassini* reaches altitudes of less than <15,000 km. The specular point trajectories and footprints of each fine-sampling cube in this section are shown in Figure 2.5 (Seignovert *et al*., 2020). A moving specular point can change the level of I/F enhancement of individual sun glitter pixels within a single cube. Accordingly, I address the specular point trajectory for each fine-sampling cube and the assumptions made on their "reliability" (i.e. ability to reasonably compare sun glitter features) in this section.

2.3.1 *Bayta Fretum*

Cassini VIMS collected hundreds of 32×1 "noodle" cubes during the T104 flyby that scanned over the entire Bayta Fretum region at a sampling of 7 km/pixel and were reconstructed with the steps outlined in Barnes *et al*. (2008). The T104 specular point moved over a distance of 35 km from the observation time of the first noodle pixel and the last sun glitter pixel (green ellipses in Figure 2.5). The travel distance is sufficiently small as to limit variations in illumination geometry of the sun glitter, so

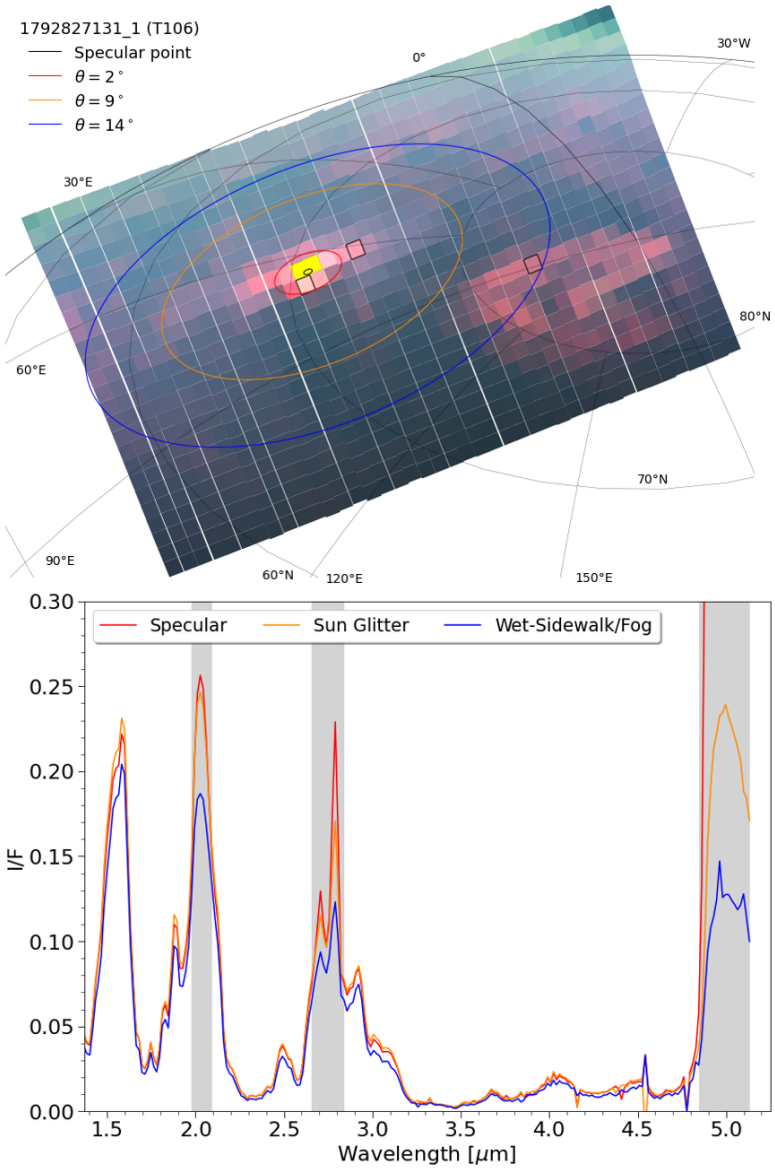

FIGURE 2.4: Top panel: The ortho-projected, saturated T106 VIMS observation with the wet-sidewalk RGB color scheme of Figure 1.6 contains both sun glitter and a wet-sidewalk feature (BEF). The ortho-projection did not use raster interpolation in order to preserve the features. The specular, sun glitter, and BEF zones are noted by red, orange, and blue ovals with their respective specular deviation angle. Yellow pixels indicate saturation. The black theoretical specular point lies within the saturated zone. Bottom panel: VIMS near-infrared pixel spectra of the corresponding features. The pixel for each zone is outlined in the top panel. Grey regions indicate the methane transmission windows.

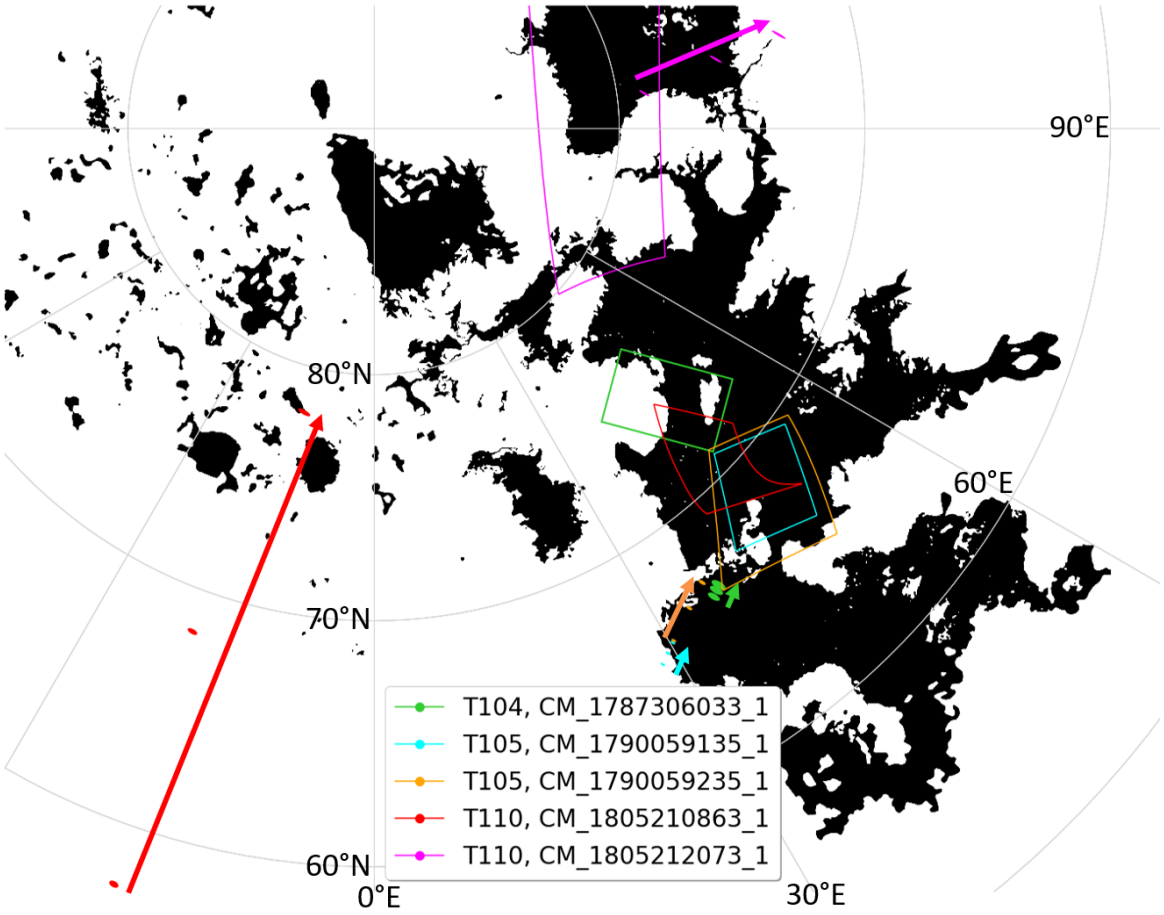

FIGURE 2.5: This figure showcases the fine-sampling VIMS cubes and their solid footprints from the T104, T105, and T110 flybys atop the binary map from Figure 2.1 in a polar projection. The colored ellipses show the relative dimensions and locations of the theoretical specular points over the observation time of the fine-sampling cubes. I plot the specular points at the start, middle, and end of the cube's observation time. The arrows indicate the direction and displacement of the specular point motion across the surface of Titan. Note that the specular point dimensions are 50 times larger for visibility, while red ellipses are 150 times larger.

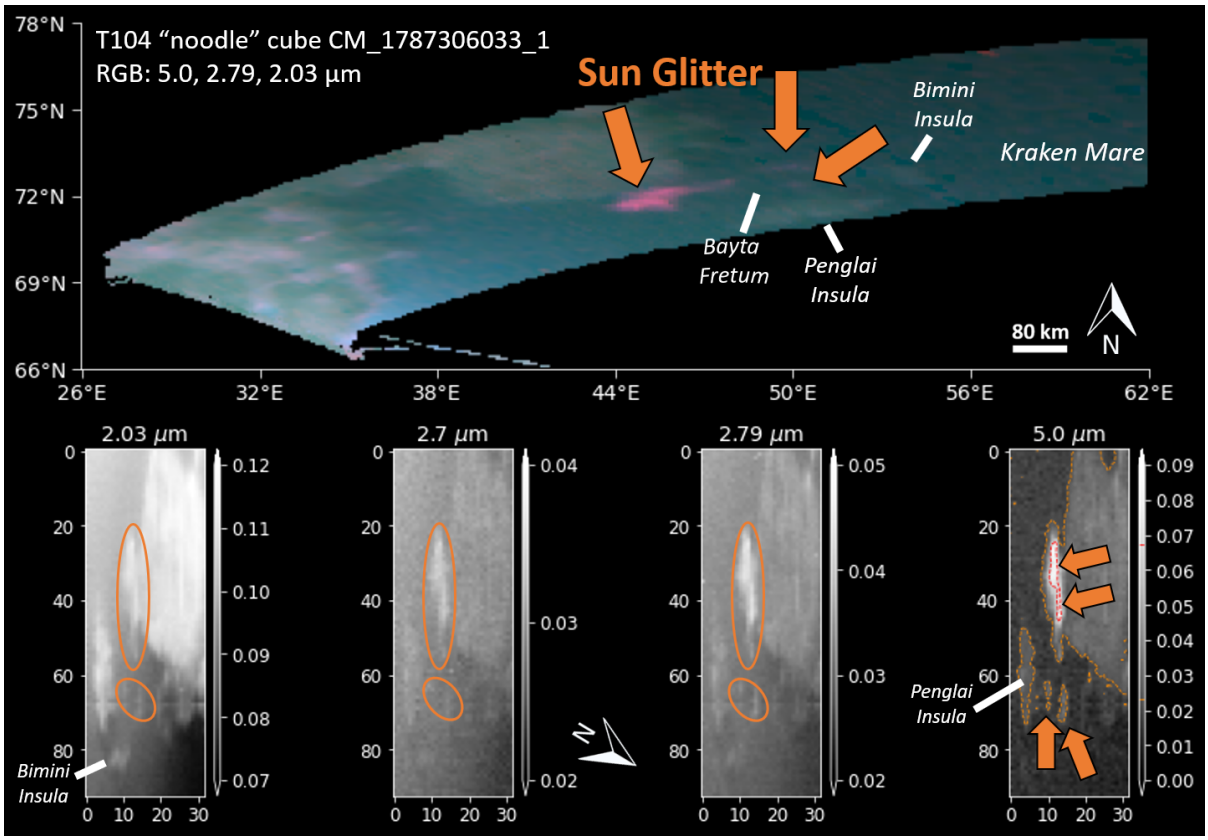

FIGURE 2.6: Top panel: A fine-sampling cylindrical map of the T104 "noodle" cube CM_1787306033_1 for northwest Kraken Mare with the same wet-sidewalk RGB color scheme as Figure 1.6. The observation reveals three separate sun glitter observations (orange arrows) in Bayta Fretum and along the northern coastline of Penglai Insula. Bottom panels: The unprojected "noodle" cube (green footprint in Figure 2.5) in the 4 transmission windows (left to right: 2.03, 2.7, 2.79, 5.0 µm) shows where the sun glitter pops out near the Bayta coastline. The 5 µm image includes red and orange dashed I/F contours of 0.023 and 0.057 respectively. The 5 µm image shows the far left orange contour as the Penglai Insula, while the smaller contours identify the three distinct sun glitter feature. The red contours identify notable wave fields in the largest sun glitter feature. At shorter wavelengths, orange ovals show the sun glitter features. The colorbar range highlights the relative transparencies of the transmission windows. Note that Bimini Insula is not visible in the 5 µm window due to its low signal-to-noise ratio (see Figure 3b of Sotin *et al.*, 2012), but clearly appears at 2.03 µm.

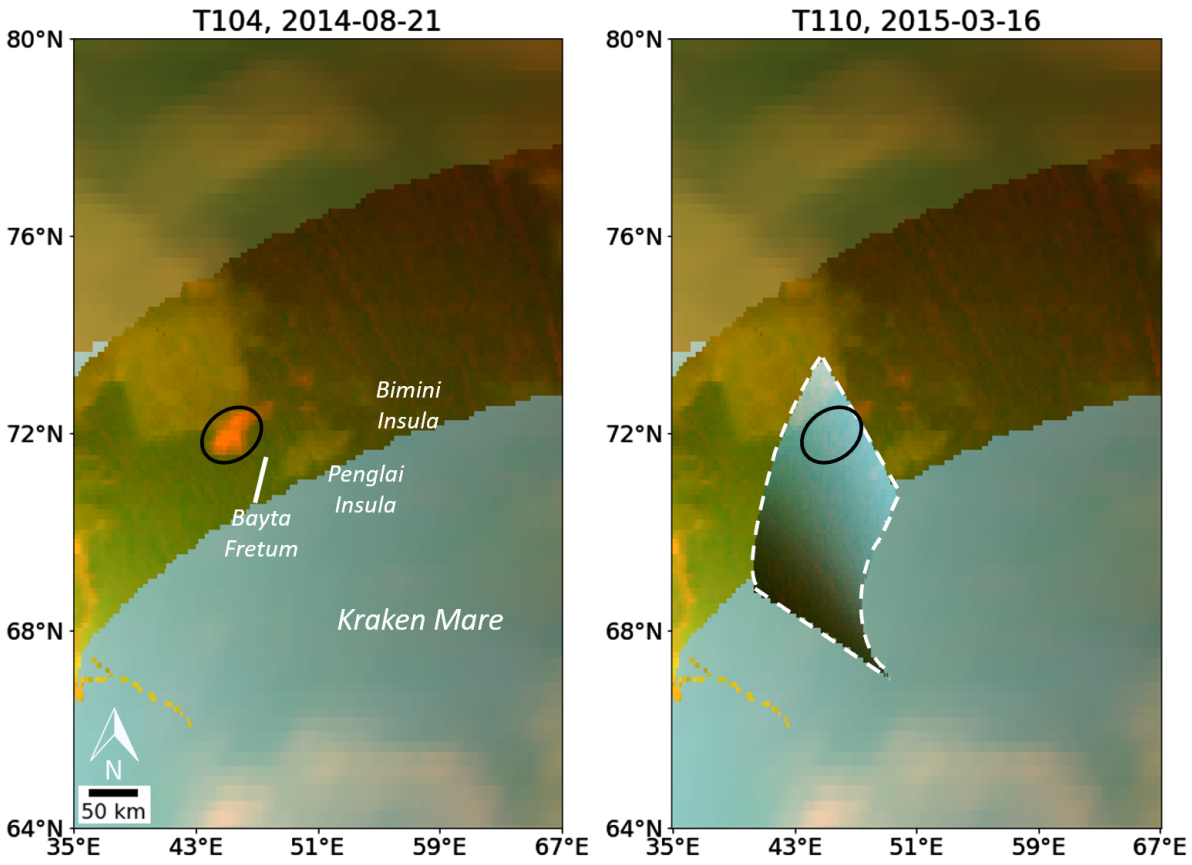

FIGURE 2.7: The left image shows the same fine-sampling "noodle" T104 cube shown in Figure 2.6 overlaid on a cylindrical basemap of northwest Kraken Mare with the same contrast-enhanced wet-sidewalk color scheme (Figure 1.6). The right image shows the VIMS cube CM_1805210863_1 (white, dashed lines) from the T110 flyby that overlies the T104 Bayta sun glitter region from the left image. The diffuse reflection on the sea is due to emission angles exceeding 60° (Vixie *et al.*, 2015). This observation shows no sun glitter during the T110 flyby in Bayta Fretum; however, the observation geometry for this cube limits our ability to rule out surface roughness.

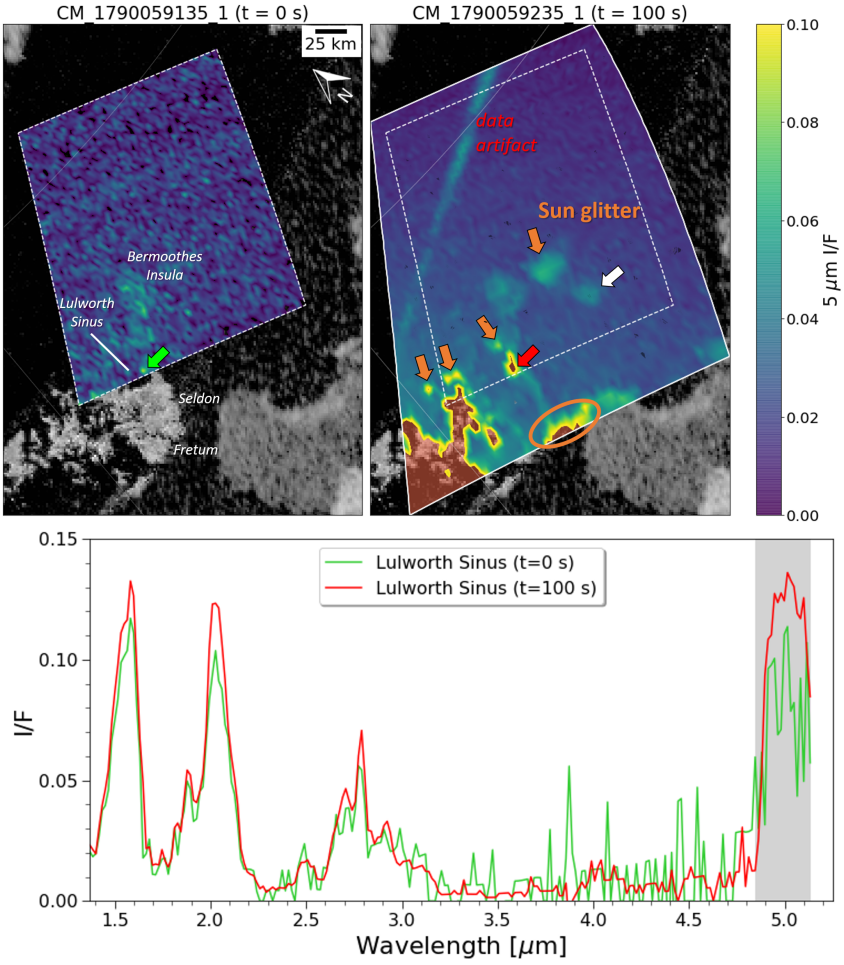

FIGURE 2.8: Two fine-sampling (~2 km) VIMS observations of sun glitter near Seldon Fretum from the T105 flyby in a polar stereographic projection overlying a *Cassini* HiSAR RADAR basemap (Lopes *et al.*, 2019a). The white outlines indicate the spatial extent of each cube. The red color indicates a 5 μm I/F greater than 0.1 that corresponds to the specular "zone" with a maximum I/F of ~0.76. These observations were taken 100 seconds apart. The second observation (t=100 s) has an 80 ms exposure time. I observe numerous instances of sun glitter (orange arrows) with the brightest ones occurring in Lulworth Sinus and Seldon Fretum (orange oval). Weaker sun glitter was detected near the north tip of Bermoothes Insula. The white arrow points to offshore sun glitter. The first cube was taken at a 20 ms exposure time, resulting in a poor signal-to-ratio for the 5 μm window. Thus, there was only one repeat detection of sun glitter between the two observations in Lulworth Sinus, based on its overall I/F enhancement at 5 μm (grey region) shown in the bottom spectral plot.

I can reasonably compare the Bayta sun glitter features. I note that the change of the spacecraft altitude is small and negligible for this observation.

Figure 2.6 displays the compiled noodle observations in wet-sidewalk color and the methane transmission windows. A cylindrical projection of the T104 noodle observation (top panel, Figure 2.6) shows a distinct coastline that correlates well with *Cassini* RADAR observations and three separate sun glitter features (orange arrows) in Bayta Fretum (Lopes *et al.*, 2019a). The two fainter sun glitter features directly north of Penglai Insula (top panel, Figure 2.6) only become visible at a higher sampling, unlike the largest linear sun glitter that represents the T104 Bayta sun glitter at moderate sampling (17 km/pixel) in Figure 2.2. Multiple sun glitter detections may imply that distinct wave fields originating from multiple sources are present in Bayta Fretum.

I comment on the largest fine-sampling sun glitter in the 4 transmission windows (2.03, 2.7, 2.79, and 5.0 μm) shown in the bottom panels of Figure 2.6. The structure of the sun glitter becomes non-uniform in the 5 μm window as seen by the red, dashed contours in Figure 2.6, which likely means that the wave field is variegated with some range of wave heights. The two brighter wave fields inside the largest sun glitter also appear at different distances between ∼10-25 km from the coastline. I determine the approximate coastline at 1.58 μm where no sun glitter is present. I also observe the sun glitter with a similar morphology in the shorter atmospheric windows at 2.03, 2.7, and 2.79 μm. Note that the sun glitter I/F intensity varies with the atmospheric transparency of each window, where shorter wavelengths are less transparent. The sun glitter I/F is independent of the sea composition since the refractive indices of liquid methane and ethane show little change over VIMS wavelengths (Martonchik and Orton, 1994), consistent with multi-wavelength sun glitter imagery of Earth's ocean (Kay *et al.*, 2009).

During the T110 flyby, *Cassini* obtained a fine-sampling (2 km/pixel) VIMS cube CM_1805210863_1 of Bayta Fretum that overlapped the largest T104 sun glitter in Figure 2.7. I note that the brightened surface on Kraken Mare is not caused by a specular reflection but rather skylight being reflected off the sea surface due to

emission angles exceeding 60° (Vixie *et al.*, 2015; refer to Figure 5 of Barnes *et al.* (2014) for a visual example). The right image of Figure 2.7 seemingly shows no evidence of surface roughness amongst the brightened sea surface in the T110 observation. On a brightened sea surface, I expect surface roughness to manifest as dark patches since they limit the number of surface facets able to reflect skylight. However, I am unable to fully rule out the possibility of surface roughness since VIMS does not have the sensitivity to distinguish darker regions on a sea surface with very low reflectance (∼1%) (Sotin *et al.*, 2012). In addition, the T110 specular point is located several hundred kilometers from Bayta Fretum (Figure 2.5), preventing the detection of any possible sun glitter.

2.3.2 *Seldon Fretum*

The 40×17 km Seldon Fretum and nearby archipelago have been suggested to play a significant role in the tidal interactions and liquid exchanges between the north and south Kraken Mare basins (Lorenz *et al.*, 2014, Tokano, 2010, Tokano *et al.*, 2014, Vincent *et al.*, 2018). Fine-sampling sun glitter imagery can therefore shed light on the sea surface dynamics of the Seldon Fretum region. As such, I present the first observational evidence of sun glitter in 2 separate fine-sampling (2-3 km/pixel) cubes, CM_1790059135_1 and CM_1790059235_1, of the immediate region of Seldon Fretum during the T105 flyby. The T105 specular point travels 115 km northeastward over the observation time of VIMS cube CM_1790059235_1 (orange ellipses in Figure 2.5). So, I do not include pixels with an I/F greater than 0.1 from the specular zone, denoted by the red region in Figure 2.8, from this cube in our analysis.

Overall, I identify six isolated instances of sun glitter in CM_1790059235_1, denoted by arrows or ovals in Figure 2.8. I overlay a *Cassini* RADAR basemap (Lopes *et al.*, 2019a) to put these instances of sun glitter into geographic context. I note that the red region likely contains sun glitter in the narrow channels between the islands.

First, I observe a notable extent of sun glitter that nearly overlays the northern terminus of Seldon Fretum (orange oval in Figure 2.8). The striking part of the

Seldon sun glitter is how it terminates at the northern edge of the strait, showing how the sea surface roughness is confined to Seldon Fretum.

Second, the entrance of a previously unnamed cove has notable sun glitter that exceeds a 5 μm I/F of 0.1 (red arrow in Figure 2.8). This cove, Lulworth Sinus, has a narrow 10 km mouth from RADAR data (Lorenz *et al.*, 2014), so the Lulworth sun glitter indicates notable sea surface roughness at the mouth. In addition, the Lulworth sun glitter was the only one likely observed in a second fine-sampling VIMS cube, CM_1790059135_1, taken only 100 seconds earlier (green arrow in Figure 2.8). The specular point distance for the Lulworth sun glitter pixel in cube CM_1790059135_1 is ∼300 km, so I can reasonably compare the Lulworth sun glitter pixels between the two T105 cubes. Unfortunately, the 20 ms exposure time of cube CM_1790059135_1 created a rather noisy observation at 5 μm (top left plot of Figure 2.8). Nonetheless, I observe an overall I/F increase in the 5 μm window for both Lulworth sun glitter pixels in their spectra in Figure 2.8. Overall, I cannot be certain of a time-resolved observation of sea surface roughness at the mouth of Lulworth Sinus without ruling out the different viewing geometry between the two cubes.

Third, I note four isolated instances of sun glitter near tiny RADAR-bright islands off the coasts of Hufaidh Insulae and Bermoothes Insula (orange arrows in Figure 2.8). The locations of this sun glitter near the coastlines of tiny islands may suggest a build-up of sea surface waves (i.e. a wave field). If this interpretation of the sun glitter is true, then the wave fields may originate from multiple sources, given their relative locations on different sides of their respective island. The rightmost sun glitter (white arrow in Figure 2.8) is not located near any visible coastline, suggesting local sea surface roughness may be caused by unseen factors, such as a submarine landmass (e.g. a seamount) disrupting a surface current.

Finally, I address the presence of a ∼100 km linear feature that appears in cube CM_1790059235_1 (denoted as "data artifact" in Figure 2.8). The specular point trajectory for the observation time of this cube is directly behind the cube's orange footprint in Figure 2.5. I also do not see this alignment or similar artifacts in any other fine-sampling VIMS observation. Thus, I attribute the feature to a sunbeam (Lynch

et al., 2001) radiating from the specular point. This artifact is similar to previous specular reflection anomalies (Barnes *et al.*, 2013b) caused by an instrumental artifact due to internal reflections in VIMS.

2.3.3 *Tunu Sinus*

The ∼20 km wide strait Tunu Sinus has also been a place of interest in regards to the fast tidal flows predicted for this portion of the north Kraken Mare basin (Tokano, 2010, Vincent *et al.*, 2018). I observe evidence of sun glitter present in Tunu Sinus in a fine-sampling (3 km/pixel) cube, CM_1805212073_1, during the T110 flyby, shown in Figure 2.9. The T110 specular point only moves 25 km southward over the observation time of the Tunu Sinus region (purple ellipses in Figure 2.5), allowing us to compare the individual sun glitter features.

Four or five unique instances of 5 μm sun glitter appear confined to the narrow straits or concave coastlines of Tunu Sinus. Specifically, I note the brightest sun glitter coincides with the narrowest (∼15 km) portions of Tunu Sinus, which may correspond to the most turbulent wave fields in this observation.

2.4 DISCUSSION

I postulate as to the possible origins of the wave fields associated with the sun glitter observations.

2.4.1 *Origin of T104 Bayta Fretum sun glitter*

Large swaths of sun glitter are common features for various coastlines of Earth from airplanes and fine-sampling remote sensing (Kay *et al.*, 2009). Deep-sea surface waves approaching a coastline experience wave-shoaling or increases in wave height from turbulent actions with the seafloor (Craik *et al.*, 2004). The wave base is the maximum depth at which a propagating surface wave can turbulently interact with the seafloor. On Earth, the wave base is considered one-half of the wavelength of a surface wave. Thus, the variegated sun glitter may indicate a shallow bathymetry for Bayta Fretum.

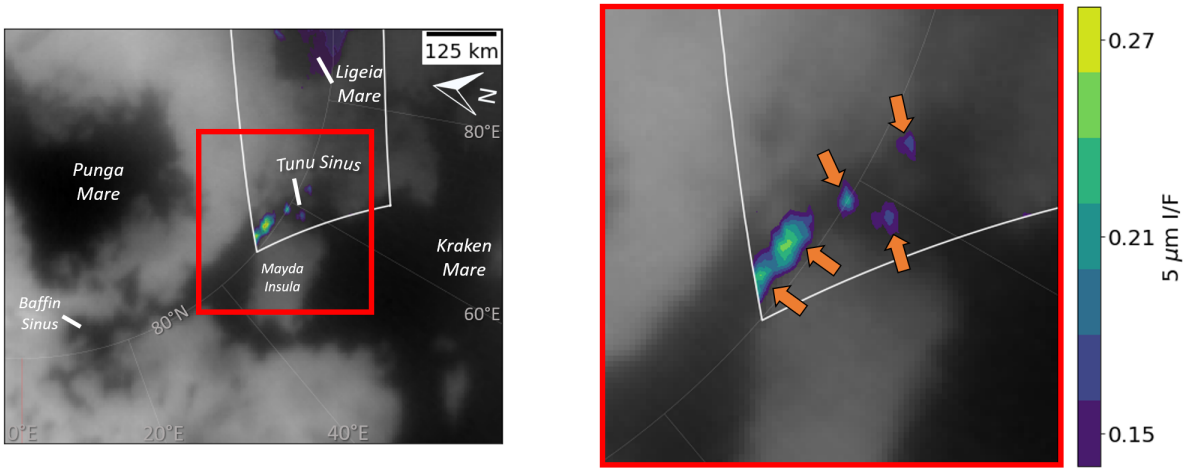

FIGURE 2.9: The left image show the 2.8 km^2 *Cassini* ISS basemap (Karkoschka *et al.*, 2017) in a polar projection with labeled features of the maria. The right plot shows an inset image (red box) of the fine-sampling (∼3 km) T110 VIMS observation CM_1805212073_1 with isolated sun glitter in Tunu Sinus at 5 μm, indicated by orange arrows. The white outline indicates the spatial extent of the VIMS image cube. The I/F range isolates the sun glitter in Tunu Sinus since the 5 μm I/F is ∼0.1 for the dark sea pixels.

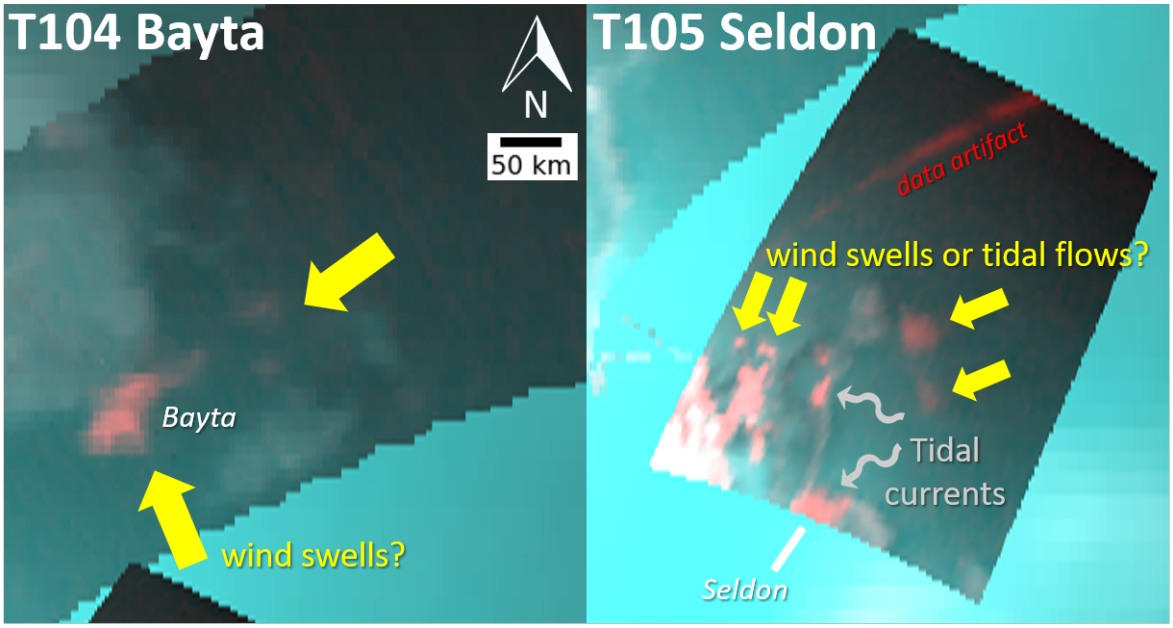

FIGURE 2.10: Summary of the possible origins of the fine sampling sun glitter and associated wave fields in the T104 noodle cube and T105 cube CM_1790059235_1. I use the same wet-sidewalk RGB color scheme of Figure 1.6. I note the linear sunbeam as the "data artifact" in the T105 cube. The arrows are not an indicator of flow direction, which remains unknown. The largest Bayta wave fields likely originate from winds given the weak tidal currents predicted in Bayta Fretum. For Seldon Fretum and Lulworth Sinus, the wave fields seem to originate from the constriction of tidal currents in their mouths. The other weaker sun glitter may originate from the winds or tides with enhancement from local areas of shallow bathymetry near the coastlines (i.e. wave-shoaling).

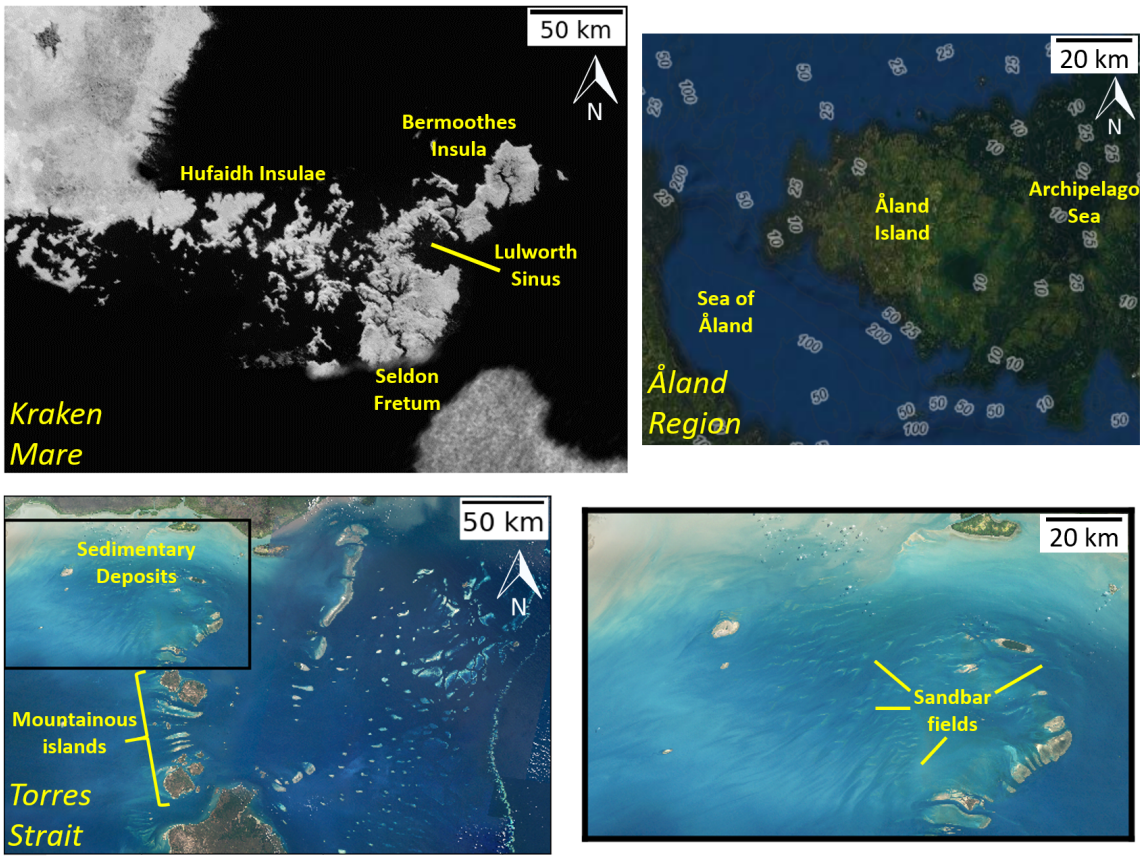

FIGURE 2.11: Two possible scenarios for the marine environment of Bermoothes and Hufaidh Insulae with terrestrial analogues. Top left panel: A cleaned *Cassini* RADAR map of Hufaidh and Bermoothes Insulae in a cylindrical projection (Credit: NASA/JPL-Caltech/Space Science Institute/Ian Regan). Top right panel: An ESRI World Imagery basemap of the Åland Region situated between Sweden and Finland with local NOAA bathymetry depths in meters. Bottom left and right panels: A compiled NASA MODIS mosaic of the Torres Strait in a cylindrical projection (Lawrey, 2013) and a subwindow of the north region (black ox) respectively. This Kraken Mare archipelago displays a similar island density and coastal morphology to the Åland Region and Torres Strait. Both terrestrial analogues host shallow bathymetry. This may imply a similar bathymetry for Bermoothes and Hufaidh Insulae if there was a recent geological period of sea-level rise or tectonic uplift. If a large sediment supply is available in Bermoothes and Hufaidh Insulae, then tidal currents may form submarine features similar to the intricate sandbars seen in the northern Torres strait (bottom right panel).

However, this explanation does not pin down the origin of the wave fields observed in Bayta Fretum. Nonetheless, I postulate two possible origins for deep-sea waves reaching Bayta Fretum with inference from applicable physical models of Titan's sea processes: 1) tidal currents and 2) wind swells.

First, tidal models of Titan have attempted to estimate the general trends of tidal surface currents in the northern maria over a Titan day (Tokano *et al.*, 2014, Vincent *et al.*, 2018). The most recent model predicts that the wider margins of Bayta Fretum might only allow for a maximum southward tidal current of 1 cm/s at perikron, Titan's closest approach to Saturn (Vincent *et al.*, 2018). This observation generally holds for several assumed bathymetric profiles (Vincent *et al.*, 2018), considering the bathymetry of Kraken Mare is mostly unknown (Hayes *et al.*, 2018). Tidal currents of 1 cm/s do not reach the 11 cm/s threshold predicted for capillary-gravity wave generation (Hayes *et al.*, 2013). Furthermore, I note that the T104 and T110 Bayta observations from Figure 2.7 were recorded at the same true anomaly, indicating diurnal tides may not be responsible for the sun glitter. As a result, a coastal tidal current likely does not explain the Bayta wave fields without an additional unknown factor, such as a local area of shallow bathymetry.

Secondly, wind-induced wave activity has been long-speculated on Titan's maria (Ghafoor *et al.*, 2000, Ori *et al.*, 1998) considering the ubiquitous occurrence of surface waves on Earth, which ranges from capillary ripples to 30 m high waves in the open ocean (Toffoli and Bitner-Gregersen, 2017). Initial laboratory experiments and several wind-wave models of Titan have found that the maximum predicted 1 m/s winds can generate capillary wind waves with meter-scale wavelengths and wave heights of $\sim$20 cm (Ghafoor *et al.*, 2000, Hayes *et al.*, 2013, Lorenz *et al.*, 2005, Lorenz and Hayes, 2012, Lorenz *et al.*, 2012). Furthermore, coupled sea-GCM models indicate relatively ethane-rich seas, like Kraken Mare, might enhance moist convection and subsequent wind activity directly over the seas (i.e. a sea breeze) (Tokano, 2009). Our moderate-sampling T104 and T105 sun glitter observations show evidence of consistently rough sea surfaces in Bayta Fretum, suggesting the possible wind source has a regional origin within the north Kraken basin.

The T104 observations of the arrow cloud located north of Ligeia Mare (Figure 2.3) and a northern Ligeia "magic island" interpreted as waves (Hofgartner *et al.*, 2016) may indicate the arrow cloud is associated with deep convective processes and stormy weather over Ligeia Mare. However, the Bayta waves are ∼700 km away from the arrow cloud. Gust fronts formed by storm downdrafts may generate surface winds of 10 m/s (Charnay *et al.*, 2015), but likely only have a radius of influence of a few hundred kilometers based on numerical storm simulations in Titan's lower troposphere (Rafkin and Barth, 2015) and terrestrial observations (Lothon *et al.*, 2011). Thus, I cannot ascertain that the arrow cloud system could have wind fields strong enough to generate wind swells out at Bayta Fretum. In addition, Bimini and Penglai Insulae may act as large breakwaters that protect Bayta Fretum from large wind swells.

Overall, the differentiation between surface waves induced by tides or wind is quite difficult with limited fine-sampling observations and observation geometries. Sea-wind circulation models show that the coastal regions of Kraken Mare may experience similar sea level changes from the tides and summer winds (Tokano and Lorenz, 2015). Specifically, the maximum wind setup (i.e. increase in sea level near the coast due to wind-wave action) is nearly equivalent to the tidal range of ∼8-10 cm on the Bayta shoreline. Thus, the combination of our sun glitter observations and model predictions suggest a complex dynamic for wave activity initiated by the winds or tides that depends on unknown coastline characteristics, such as bathymetry (Hayes *et al.*, 2018).

2.4.2 *Origin of T105 Seldon Fretum sun glitter*

Seldon Fretum is a narrow strait connecting the two large basins of Kraken Mare expected to host choppy seas (Lorenz *et al.*, 2014).

Tidal Currents: Seldon Fretum and Lulworth Sinus — The most noteworthy sun glitter detection in the fine-sampling T105 cube CM_1790059235_1 were in Seldon Fretum and the entrance of Lulworth Sinus. Seldon Fretum is the

location where fast northward tidal currents are predicted in tidal models at ∼0.2 Titan days after apokron (Tokano *et al.*, 2014, Vincent *et al.*, 2018). The tidal models assumed shallow bathymetric profiles (<50 m) for Seldon Fretum and Lulworth Sinus, based on the idea that depth scales with distance from the shoreline (Lorenz *et al.*, 2014). Thus, I find the sun glitter in these regions consistent with tidal currents constricted at the strait entrances that manifest as turbulent sea surfaces. I quantify the possible sea surface roughness in these narrow straits. The Reynolds number helps describe the type of flow for a liquid in a channel, given by:

$$Re = \frac{4uA}{\nu P} \tag{2.1}$$

where u is the flow speed, A is the channel cross-sectional area, P is the wetted perimeter, and ν is the kinematic viscosity. If I assume a rectangular channel width and depth of 20 km and 50 m respectively with liquid methane flowing at decimeter-scale tidal current velocities predicted in models (Vincent *et al.*, 2018), Seldon tidal currents easily reach the turbulent flow regime ($Re > 2300$). Also, energy balance ($gh = 0.5u^2$) shows that 0.3 m/s tidal current velocities (u) in Seldon Fretum can cause a sea surface roughness (h) of ∼3 cm, reaching the capillary-gravity wave threshold (Hayes *et al.*, 2013). The surface liquid exchanges between the Kraken basins would be driven by tidal flows with only minor influences from surface winds in Seldon Fretum (Lorenz *et al.*, 2014, Ori *et al.*, 1998). I anticipate a spectrum of centimeter-scale wave heights in Seldon Fretum, but constraining wave heights remains beyond the scope of this work without bathymetric profiles.

The occurrence of internal waves, the surface manifestations of turbulence at the boundary of two stratified layers in the sea, has been suggested for Seldon Fretum due to the possibility of stratified seas (Lorenz *et al.*, 2014). Recent theoretical and experimental evidence shows one possible scenario for a two-liquid layer stratification with a methane-rich top layer and an ethane-rich bottom layer in Kraken Mare (Cordier *et al.*, 2017, Hanley *et al.*, 2018). If this binary liquid were present in Seldon Fretum, then tidal currents in the top methane-rich layer could cause roughness on the bottom ethane-rich layer and subsequently generate internal waves

that propagate to the surface at some distance from Seldon Fretum. However, if Seldon Fretum has shallow bathymetry, I note that any stratification may be broken due to significant mixing from the bottom friction of the seafloor. On Earth, there is a lack of internal waves in certain straits, such as the English channel (Jackson, 2007). Alternatively, a shallow Seldon Fretum may only allow for the exchange of the surface methane layer, also preventing internal wave formation.

Surface waves: Bermoothes and Hufaidh Insulae — The coarse sampled T105 cube in Figure 2.2 shows a large swath of the surface of north Kraken Mare being roughened, which I interpret as windy surface conditions over Kraken Mare on this Titan day. The 4 separate detections of sun glitter along the northern shores of Bermoothes and Hufaidh Insulae (orange arrows in Figure 2.8) have two possible origins: winds or tidal currents. In practice, distinguishing between the two is quite hard from a single sun glitter observation. I am likely only observing a small part of the actual wave angle spectrum that is limited by our viewing geometry bias. I note that one sun glitter feature is located $\sim$30 km offshore of Bermoothes Insula (white arrow in Figure 2.8), which may indicate wind-roughened seas in Kraken Mare. The red regions over Hufaidh Insulae in Figure 2.8 are likely indicative of surface waves generated from constricted tidal currents. Overall, I cannot determine a single origin for these Insula wave fields but rather likely originate from a combination of the tides and summer winds.

Coastal Morphology of Hufaidh and Bermoothes Insulae — I can interpret the coastal morphology and geology of Hufaidh and Bermoothes Insulae using the observations of various wave fields in the Seldon Fretum region. I identify two potential terrestrial analogues to this region: the Åland Region in the Baltic Sea (Lorenz *et al.*, 2014) and the Torres Strait between Australia and Papua New Guinea. These terrestrial analogues are both island-dense straits with shallow bathymetry ($<$25 m) but different sediment supplies available in their submarine environment.

First, the $\sim$160 km wide Torres Strait that divides the north tip of Queensland, Australia and Papua New Guinea shows an array of islands, more densely-populated

in the south, and sediment-rich region to the north in the bottom panels of Figure 2.11. The Torres Strait demonstrates some of the most complex tidal circulation trends on Earth from the interactions of two distinct ocean basins with different general circulation patterns and mean sea levels (Lemckert *et al.*, 2009, Wolanski *et al.*, 1988). In addition, the bathymetric profile of the Torres Strait ranges from 7-15 meters (Harris, 1988). The complex tidal currents and shallow bathymetry result in highly localized variations in wave activity in the Torres Strait (Hemer *et al.*, 2004), which may be an analogous scenario for the straits of Hufaidh and Bermoothes Insulae. The tidal action becomes apparent from the wave-like bedforms, such as sand waves (Daniell, 2015, Pilkey *et al.*, 2011) in the bottom right image of Figure 2.11, analogous to sand dunes sculpted by the winds. I suggest a version of "icy" sandbars as an intriguing possibility for the submarine environment of Hufaidh Insulae, previously postulated by Lorenz *et al.* (2003) and Lorenz (2013). This scenario would only hold if there was a large sediment runoff from nearby rivers dumping into Kraken Mare (Burr *et al.*, 2006, Ori *et al.*, 1998).

Second, the Åland region has been suggested as a terrestrial analogue to Hufaidh Insulae, Bermoothes Insula, and Seldon Fretum (Lorenz *et al.*, 2014). The top right panel of Figure 2.11 shows the Åland region and equivalent Titan features, where the Sea of Åland is Seldon Fretum, the Åland Island is Bermoothes Insula, and the Archipelago Sea is Hufaidh Insulae. I observe complex daily surface circulation patterns in the Archipelago Sea (Erkkilä and Kalliola, 2004) with shallow depths (Figure 2.11), which may share the circulation patterns of the Hufaidh Insulae straits. The Sea of Åland often hosts choppy seas (Kahma *et al.*, 2003), which may resemble the wave conditions of Seldon Fretum. Meanwhile, the Åland and Archipelago Sea islands host a mix of cliffed and ria/flooded coastlines in a similar manner to Bermoothes and Hufaidh Insulae respectively. However, the key difference from the Torres Strait is the lack of sedimentary deposits and subsequently no submarine bedforms.

For the actual islands of Hufaidh and Bermoothes Insulae, geomorphological analysis shows the region is likely composed of the hard primordial crust that predates

the hydrocarbon seas (Birch *et al.*, 2017). The rugged, sinuous coastlines and internal river valleys may resemble the submergent coastlines of Earth with rias or flooded coastal inlets (Bird, 2011). The rugged coastlines suggest a slow erosion rate of the Insulae, similar to the erosional history of Mayda Insula (Lucas *et al.*, 2014). The submergent coastlines of Hufaidh and Bermoothes Insulae might also hint at a similar geological history to the two terrestrial analogues. For the Torres Strait, the local peaks of the southern Torres Strait islands were likely isolated from rising sea levels after the Last Glacial Period (Glover, 1977). For the Åland Region, the hard granite islands likely rose out of the sea due to post-glacial isostasy from the last ice age (Edelman and Jaanus, 1980). Thus, the local peaks in the Hufaidh and Bermoothes Insulae may originate from either: a period of sea-level rise or tectonic uplift of an erosion-resistant bedrock.

One final geological feature is the semi-circular Lulworth Sinus. The observation of bright sun glitter at the entrance to Lulworth Sinus in two separate T105 cubes indicates tidal currents and considerable wave activity in Lulworth Sinus. The interior coastlines appear to host several rias in Figure 2.11, suggesting that Lulworth Sinus was likely infilled during a period of sea-level rise or isostatic subsidence. Thus, wave action likely has not played a role in the formation or semi-circular shape of Lulworth Sinus.

2.4.3 *Origin of T110 Tunu Sinus sun glitter*

Stereo topography of the nearby Mayda Insula from *Cassini* RADAR suggests significant fluvial erosion of the terrain (Lucas *et al.*, 2014). Tidal models of Titan predict decimeter-scale tidal flow velocities in the Tunu Sinus region (Tokano *et al.*, 2014, Vincent *et al.*, 2018). I suggest that the sun glitter likely originates from the constriction of tidal currents flowing into the narrow straits and concave coastlines of Tunu Sinus. I am unable to rule out the influence of winds without an observation of local weather conditions during the T110 flyby due to the high phase angle. Fluvial erosion may be an ongoing geological process driven by tidal flows in the coastal areas of Tunu Sinus (Ori *et al.*, 1998). The observation of active tidal currents in Tunu

Sinus, combined with evidence for the Maria sharing an equipotential surface (Hayes *et al.*, 2017), may also indicate active hydrological connections between Kraken and Punga Maria via surface channels currently unresolved by RADAR.

CHAPTER 3

Punga Mare Sun Glitter Observations[3]

I wrote this chapter on the suggestion of my advisor after I had discovered this T110 VIMS cube of Punga Mare in my search for interesting surface anomalies in the sunglint images throughout the VIMS database. Once my advisor realized that I had stumbled upon new sun glitter features with different morphologies and locations around Punga Mare in this VIMS cube, I pursued a further investigation on each specular feature and possible hypotheses for them. We are currently going through peer review on the publication of the results from this chapter in the *Planetary Science Journal*.

3.1 DATA & SURFACE CONTEXT

On *Cassini's* T110 flyby on 16 March 2015, VIMS acquired particularly high-quality fine-resolution 64 x 64 cube, CM_1805211625_1, that shows Punga Mare in near-specular geometry. The phase angle and spatial sampling of this observation were 126° and 2.3 km pixel^{-1} respectively (Table 3.1). Relative to previous VIMS observations of Punga Mare, only cube CM_1721848119_1 from T85 has a higher phase angle of 148° (Barnes *et al.*, 2014). CM_1721848119_1, however, had a lower spatial sampling (16 km pixel^{-1}). Both have similar exposure times, 70 vs 80 milliseconds, each of which are sufficient for a high signal-to-noise ratio (Sotin *et al.*, 2012). These are the only two VIMS observations to show specular reflections on Punga Mare. Limited high-inclination polar orbits and the Sun being down early in the *Cassini* mission (Roe, 2012) explain the lack of additional observations. CM_1721848119_1 shows very little contrast between land and liquid surfaces, even in the clearest spectral channels, making it difficult to determine whether sun glitter was present (Barnes *et al.*, 2014).

[3]Significant work from this chapter was going through the peer review process for publication in the Planetary Science Journal.
Heslar M.F. & Barnes J.W. 2022 *Planetary Science Journal*. (under review)

The T110 observation, however, shows a more noticeable contrast between land and liquid surfaces. These observations merit further exploration.

I show Punga Mare and the surrounding environments in the north polar regions at 2.0 μm in the VIMS mosaic (Figure 3.1). Punga Mare is the smallest named sea on Titan. It is surrounded by even smaller lakes to the west and Kraken and Ligeia Maria to the south and east with no established hydrologic surface connections (Hayes, 2016). For the unprojected color image at right in Figure 3.1, I use the three most transparent surface windows (Barnes *et al.*, 2013b), in order of decreasing transparency (5.0, 2.8, and 2.0 μm) for the RGB color scheme. I follow the empirical atmospheric correction described in Le Mouélic *et al*. (2019b) to remove some effects of the changing viewing geometry (e.g. incidence angle) across the cube.

The intriguing bright cyan and pink surfaces in this image of Punga Mare (Figure 3.1) are caused by intense reflections of sunlight and skylight at a high phase angle of 126° (Vixie *et al.*, 2015). At high phase, the contrast between sea and land inverts, with the seas appearing brighter due to the specular reflection of sky brightness. I note that the liquid surfaces are also brighter in the T110 observation than in lower-emission-angle observations (background mosaic at left in Figure 3.1). The rougher land surfaces appear darker than the sea at higher phase angles because the land's diffuse reflections send light in all directions, leaving less brightness at high emission angles than in the sea's directional specular reflections. The isolated pink, white, and purple features scattered across the color image therefore relate to the variable properties of Punga Mare's liquid surface, which I call these unexpected areas specular features.

Sinuous coastlines and island chains are seen in the T110 observation (Figure 3.1). In Figure 3.2, a projection of the T110 observation's footprint onto a VIMS-RADAR composite map shows major overlap with the areas of Punga Mare between the RADAR and VIMS imagery. I note the coastline positions of the north-polar seas only appear to remain constant in *Cassini* Synthetic-Aperture RADAR (SAR) observations. Assuming the best SAR resolution of 1 km, I could only detect a shoreline shift with a very large 1 m drop of sea level (Hayes *et al.*, 2011), making it very unlikely to observe

coastline changes. The fine-sampling RADAR view of Punga shows numerous bays, rivers, coastal inlets, and labyrinthi that are indicative of flooded coastlines similar to the larger northern seas (Hayes, 2016).

I include relevant named features and polar-projected VIMS pixels for each anomalous sea surface feature from the T110 observation in Figure 3.2. In particular, the VIMS pixels of the specular features appear to overlap locations of notable fluvial and coastal features in the T29 SAR images of Punga Mare. The overlap of the specular features with coastal regions suggest that the specular features originate from the surface. For example, the faint purple feature in the top right corner of Figure 3.1 overlaps the channeled terrain of Ipyr Labyrinthus (Malaska *et al.*, 2020) and a reported VIMS evaporitic deposit (MacKenzie and Barnes, 2016).

Nonetheless, the specular features could also be tropospheric phenomena (e.g. clouds) or image artifacts (e.g. hot pixels caused by camera overexposure), but I rule out such possibilities. I find no evidence for a systemic presence of hot or even cosmic ray pixels across all band images of the T110 observation. The exposure time of 70 milliseconds (see Table 3.1) is well within the range of exposure times from other published specular observations (Barnes *et al.*, 2014; Dhingra *et al.*, 2020; Heslar *et al.*, 2020). Select VIMS bands, including the 2.9 μm window and the wings of the 2.03 μm window, are typically used to diagnose the presence of low-altitude clouds (Turtle *et al.*, 2018; Dhingra *et al.*, 2020). In addition, reports on specular VIMS observations pointed out key spectral distinctions between clouds, coastal evaporites, bedrock, and specular features (Dhingra *et al.*, 2019; Heslar *et al.*, 2020). Furthermore, *Cassini* cloud surveys of VIMS and ISS datasets only document clouds between 50-60°N during the T110 flyby (Turtle *et al.*, 2018). Lastly, I observe a lack of brightened features in the 2.03 μm window image (see left panel of Figure 3.1), consistent with previous findings of possible rough seas in a similar high-phase VIMS observation of Punga Mare (Barnes *et al.*, 2014).

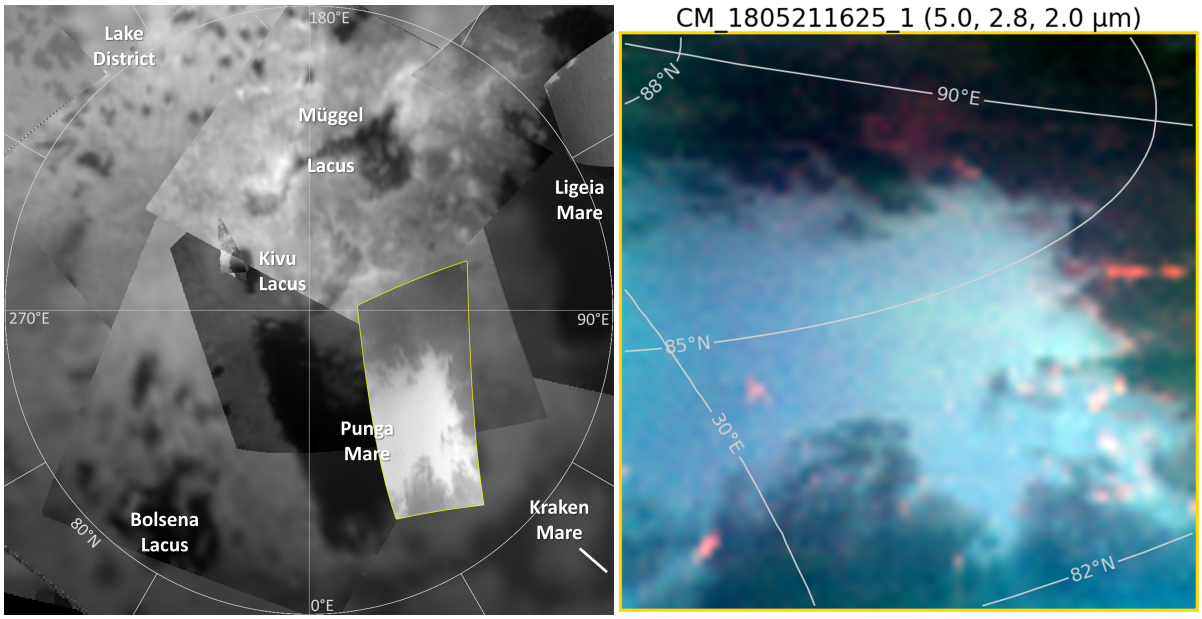

FIGURE 3.1: Left: 2.0 µm polar stereographic mosaic of Titan's north polar region above 80°N from *Cassini* Visual and Infrared Mapping Spectrometer (VIMS) observations corrected for airmass and spatial sampling. The T110 observation (CM_1805211625_1), denoted by a yellow outline, shows inverted surface reflections where sea surfaces become brighter than the rougher land due to the high phase angle (126°). Right: Unprojected VIMS color composite (RGB: 5.0, 2.8, 2.0 µm) of the T110 observation with a superimposed geographic grid. Anomalous sea surface features of interest are pink and purple.

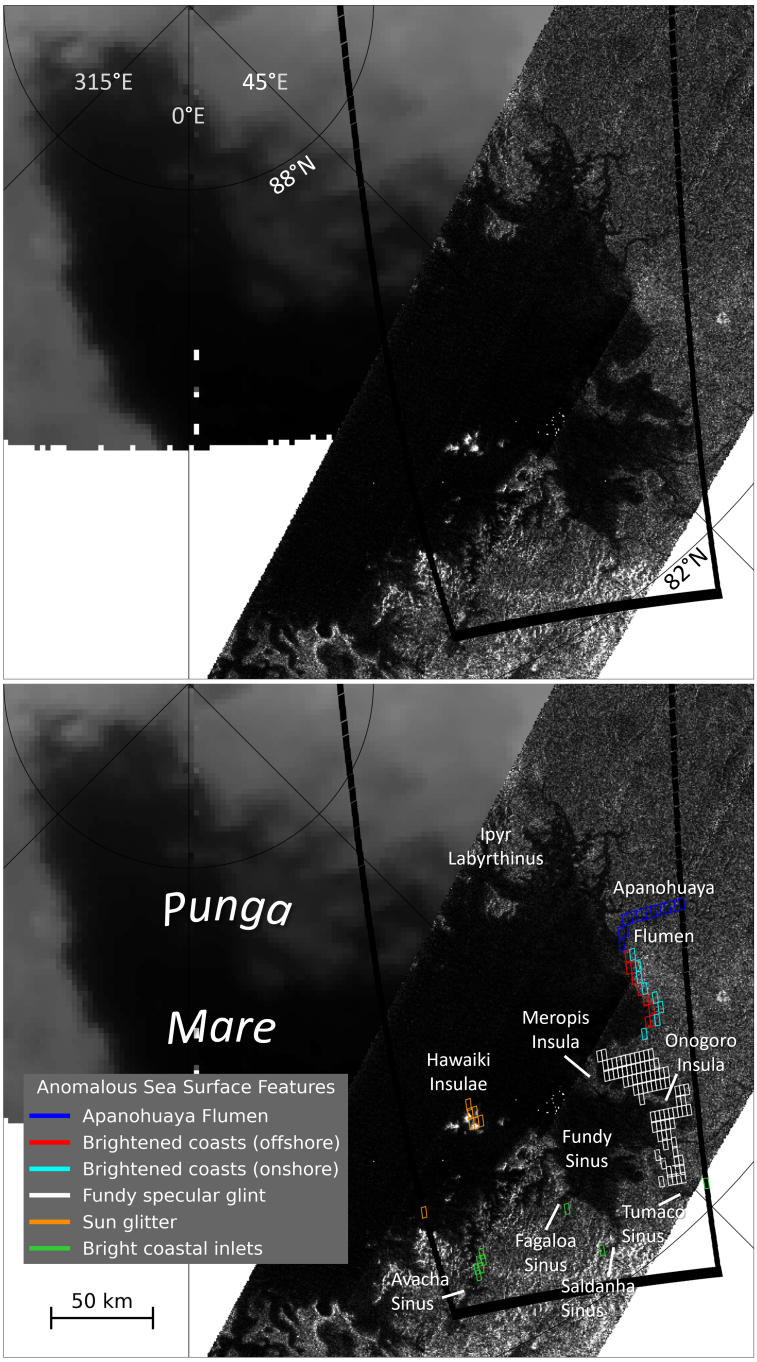

FIGURE 3.2: Top: North polar composite of Punga Mare using T29 SAR swaths and VIMS cube CM_1753530947_1. The wide black lines show the geographic extent of the T110 observation. Bottom: Same composite of Punga Mare with IAU-approved names of relevant geographic features, namely bays, channels, islands, and labyrinthi. Dark and grey pixels indicate liquid and land surfaces respectively. The composite includes projected VIMS pixels for the specular sea surface features from the T110 observation.

TABLE 3.1: Parameters of relevant VIMS observations. I use fine-sampling observations of the north polar Punga-Kivu region to identify narrow fluvial features. SC Alt. is shorthand for spacecraft altitude.

Flyby	Cube	Exposure Time [ms]	Sampling [$km\ pixel^{-1}$]	Phase [°]	Incidence [°]	Emission [°]	Airmass	SC Alt. [km]
T85	CM_1721848119_1	80	16.7	148	59-88	60-89	7.33-75.12	33,000
T93	CM_1753530947_1	300	6.6	85	62-75	11-33	3.35-4.98	15,765
T110	CM_1805211625_1	70	2.3	126	59-67	62-66	4.20-4.71	6,239

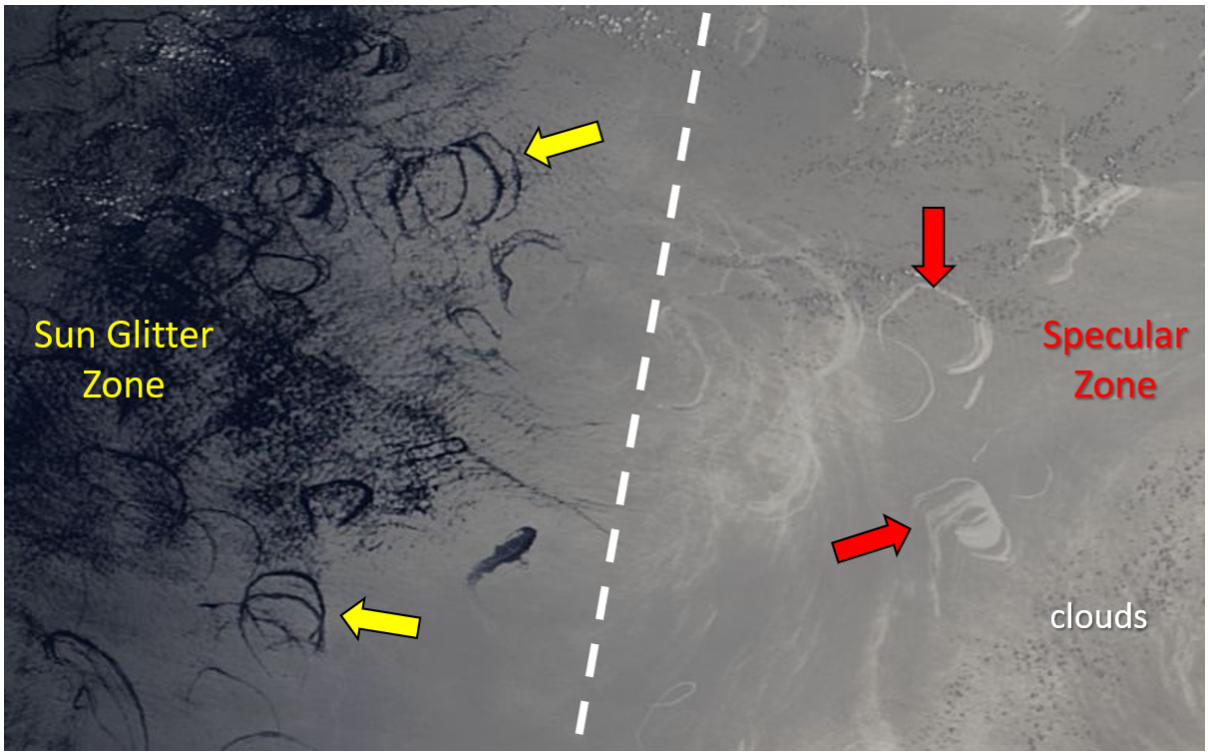

FIGURE 3.3: NASA Moderate Resolution Imaging Spectroradiometer (MODIS) true color image of natural oil seeps in the Gulf of Mexico on June 2, 2005. The silvery background shows the sea surface roughened by a constant wind. The white dashed line separates the two key zones of a terrestrial sunglint reflection: the specular and sun glitter zones. The specular point is located off the right side of the image. Arrows point to anomalous, wind-shaped oil slicks that dampen surface waves. In the specular zone, oil slicks appear brighter than the sea surface. In the sun glitter zone, oil slicks appear darker than the background. Note that clouds and their shadows dot the image.

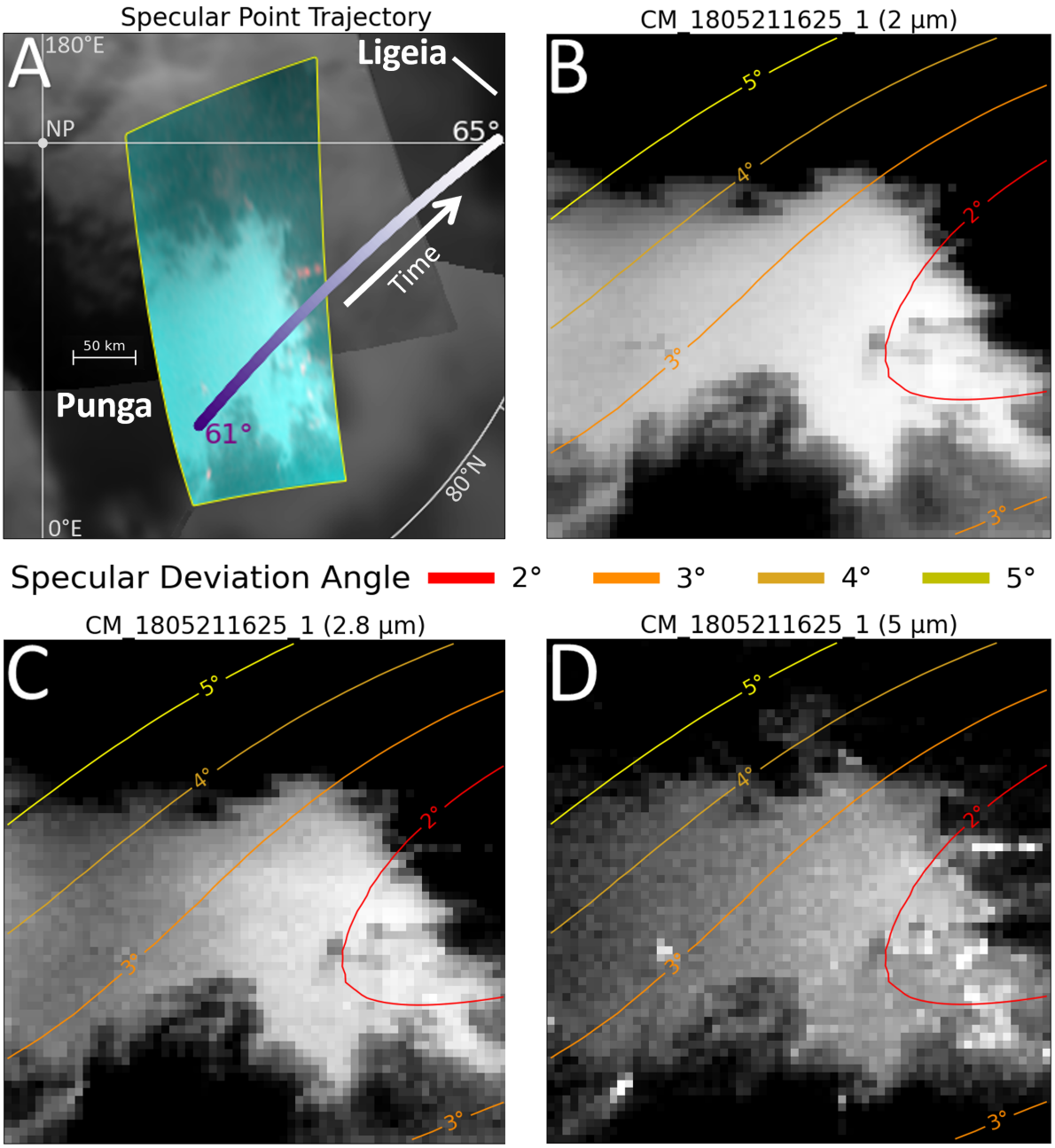

FIGURE 3.4: The top left panel shows the path and specular angle (purple to white gradient) of the solar specular point across Titan's north pole during the acquisition time of the T110 observation (5 minutes). The asymmetric distribution of the specular deviation angle is shown on the unprojected T110 observation at 2 (top right), 2.8 (bottom left), and 5 (bottom right) microns respectively. The specular and inner sun glitter zones are within 2° and 5° respectively.

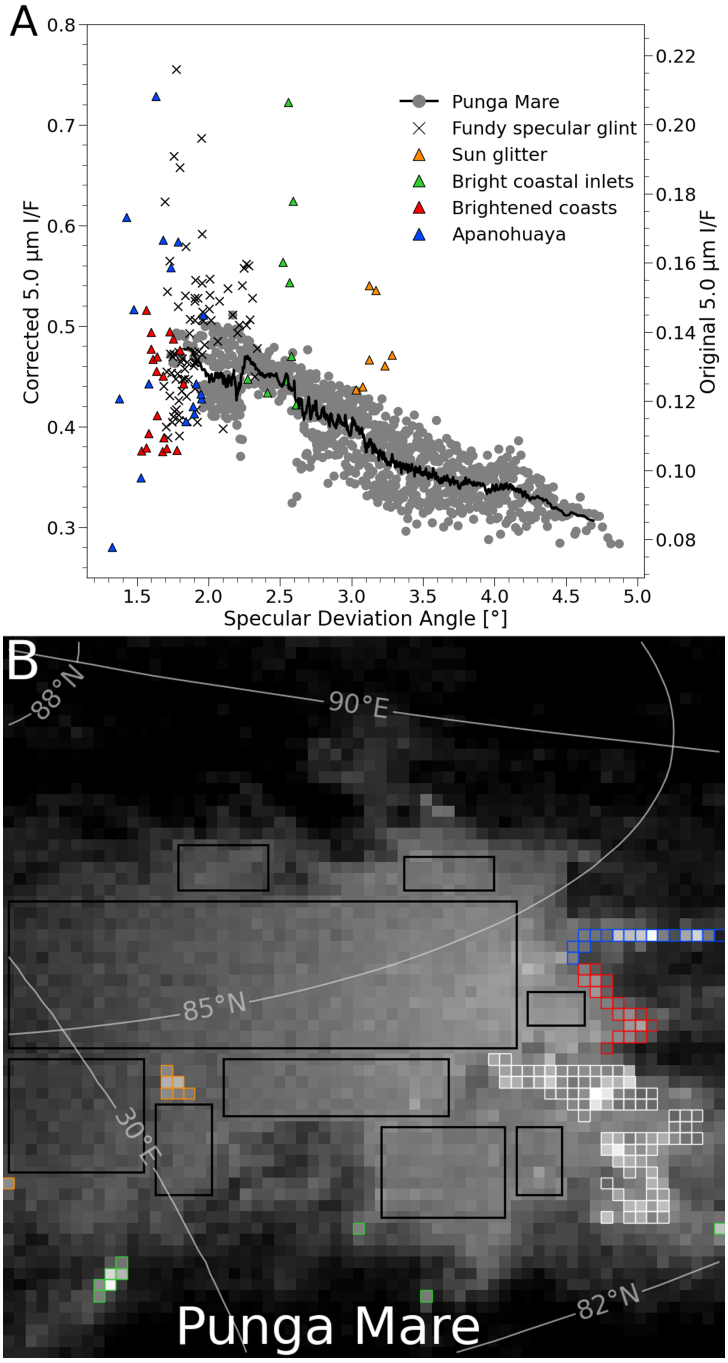

FIGURE 3.5: A) Scatter plot of 5 µm I/F (original and corrected values) and specular deviation angle for the specular sea surface features and Punga Mare, denoted by colored triangles and grey dots respectively. The solid black line indicates the 15 point moving average of those pixels that I consider to be background Punga Mare. B) Unprojected T110 observation at 5 microns with a superimposed geographic grid. I indicate the Punga Mare pixels (grey dots in plot A) with black boxes. I denote the pixels of the specular sea surface features with colored pixel borders. I/F is the ratio of observed to incident flux measured by the Cassini VIMS.

3.2 SPECULAR VIEWING GEOMETRY

Determining the nature of each anomalous sea surface feature is quite difficult when applied to spectral images at different phase angles. However, remote sensing tools and knowledge of the viewing geometry of the T110 observation can be used to limit the number of possible physical explanations for each feature.

Locating anomalous features relative to the theoretical specular point is important to determine their roughness (Jackson and Alpers, 2010). I denote feature locations by the specular deviation angle or the angular distance of a local facet from normal if it were to be in a specular geometry. The specular point corresponds to a specular deviation angle of zero degrees. Given Titan's radius of 2,575 kilometers, one degree on Titan is approximately 45.1 kilometers at 85°N (Zebker *et al.*, 2009).

I observe two distinct zones in specular reflections from the liquid bodies of Earth (Jackson and Alpers, 2010; Munk *et al.*, 2000): the specular zone and the sun glitter zone. The brightness of anomalies on the sea surface (e.g., waves) can change dramatically between these two zones. Another important factor to consider is the roughness of the background sea surface. Sea surface features that are smoother than the background sea surface appear brighter in the specular zone. Smoother sea surface features appear darker in the sun glitter zone. Conversely, sea surface features that are rougher than the background sea surface appear darker in the specular zone. Rougher sea surface features appear brighter in the sun glitter zone.

In Figure 3.3, a NASA satellite sunglint image of natural petroleum seeps manifesting on the Gulf of Mexico highlights the sharp transition of the specular and sun glitter zones and its implication on the appearance of sea surface phenomena. The white dashed line defines the transition between the specular and sun glitter zones. In the Gulf of Mexico example, I see a grey background of uniformly somewhat rough sea surface in both sun glitter and specular zones (left and right sides of Figure 3.3 respectively). The darker surfaces at left and brighter surfaces at right are the same arcuate feature. Arrows in both zones point to equivalent instances of the same feature of smooth, wave-dampening oil slicks (Ermakov *et al.*, 2019), despite their contrasting appearance. Thus, knowing the location of the zone transition is key to interpreting

the roughness of anomalous sea surface features in the T110 observation. In the specular zone at right, the smooth oil slicks preferentially reflect light towards the observer, making them stand out as bright against the grey roughened background. But at left, in the sun glitter zone, the smooth oil slicks preferentially reflect light to areas away from the observer, leaving them to appear darker than the rough grey background.

While sunglint appears similar on Titan, the sizes of the specular and sun glitter zones differ from those on Earth, which originate from differences in the observed background sea surface on Titan and Earth. On Earth, prevailing surface winds drive a continuously dynamic sea surface on most seas and oceans (Young, 1999). Meanwhile, the northern sea surfaces on Titan are mostly quiet and millimeter-smooth in early summer RADAR observations (Grima *et al.*, 2017). What I observe as sunglint on Titan is specularly reflecting sky brightness on a glass-smooth sea surface. Thus, the size of the specular zone effectively shrinks to zero and only leaves the sun glitter zone. As a result, I can interpret every bright sea surface feature as rough and dark sea surface feature as smooth.

Second, the hyperbolic orbital trajectory of *Cassini* during the 5-minute T110 observation complicates the geometry of the specular and sun glitter zones. *Cassini* typically observes specular reflections and circular solar aureoles at spacecraft altitudes of 10-100 Titan radii (Heslar *et al.*, 2020). In that case, the specular point moves only a few kilometers (i.e., less than the VIMS pixel size) during the observation time, thus, *Cassini* can capture a nearly static surface image. In contrast, *Cassini* recorded the T110 observation at a spacecraft altitude of 2 Titan radii (Table 3.1) and had a greater orbital speed. As a result, the specular point traverses over 300 kilometers from south Punga to northwest Ligeia over the 5 minutes during which the image cube is acquired (Figure 3.4). Further, the specular deviation angle contours overlaying the unprojected T110 observation in the surface windows are irregular. Note that I do not observe the specular point, coming as close as a minimum specular deviation angle of 1.28°. The larger specular deviation angle contours overlapping the darker surfaces of Punga Mare are consistent with previous

sun glitter observations (Heslar *et al.*, 2020). I see the anomalous features only at 5.0 μm and observe clearer delineations in the coastlines at 2.0 and 2.8 μm in Figure 3.4.

3.3 SPECULAR FEATURES

I term all of the unexpected, bright pixels that I see on what would normally be the dark Punga Mare "specular features". I identify 2 different classes of specular features, one of which occur within an inland channel system (Apanohuaya Flumen) and the other which occur at different locations on the sea surface. On the sea itself, I note features within the bays and near-shore coves at the southern sea margin and broader sun glitter effects that occur throughout the sea's interior. In the following subsections I describe each of these specular features in turn, along with constraints on their possible origin and the implications of their observation.

3.3.1 *Surface Brightness Profile*

I start by inspecting the background sea surface brightness of Punga Mare and the relative brightness of the specular features. Figure 3.5A shows the nearly transparent 5 μm window (Sotin *et al.*, 2012) brightness profile of Punga Mare in the sun glitter zone relative to the Fundy specular glint and anomalous features. I first note a steady increase in the mean 5 μm brightness of the Punga Mare sea surface (black line, Figure 3.5A) from specular deviation angles between 2.25° and 5°. Then, a region of Punga pixels of variegated 5 μm for specular deviation angles of 1.4-2.25°. This region of variegated 5 μm pixels visually corresponds with an area of white-pink anomalies in Figure 3.1, labelled "Fundy specular glint" (Figure 3.5), across the eastern half of Fundy Sinus. In Figure 3.5A, the white-pink anomalies within the area of the Fundy specular glint are the brightest surfaces juxtaposed to darker Punga Mare pixels. Thus, the Fundy specular glint may indicate the background sea surface brightness within 2.25° or 90 km of the specular point is sensitive enough to detect sea surface roughness.

3.3.2 *Apanohuaya Flumen*

Apanohuaya Flumen is a separate but independently notable channel feeding Punga Mare that shows a spectrally distinct brightness that led us to identify it as an anomalous specular feature. Apanohuaya Flumen was first identified in fluvial network surveys of Titan (Burr *et al.*, 2013). In Figure 3.1, I observe Apanohuaya Flumen as a bright pink linear feature within the specular zone. In Figure 3.5A, there is a large range of 5 μm I/F values for Apanohuaya, similar to the Fundy specular glint pixels, which likely indicates the Apanohuaya pixels may be sampling liquid surfaces. Thus, I split the Apanohuaya pixels into two groups: "dark" and "bright". The bright Apanohuaya pixels may correspond to a relative linear increase in liquid fill fraction from a minimum threshold. Meanwhile, the dark pixels may be below the minimum liquid fill fraction threshold, yielding no detectable I/F contribution from the specular reflections of a liquid surface. Oddly, the bright Apanohuaya pixels are brighter than most of Punga Mare at 5 μm only, as shown in the spectra of Figure 3.6. Enhanced surface reflectance or atmospheric forward scatter from liquid surfaces closer to the specular point, relative to Punga Mare, likely explain the bright Apanohuaya pixels.

I also consider how the Apanohuaya VIMS pixels overlap the observed channel in RADAR and bathymetry data in a polar projection (Figure 3.6). The wider coastal segment of Apanohuaya Flumen closest to Punga Mare shows an overlap only with the "dark" Apanohuaya pixels. Meanwhile, the "bright" Apanohuaya pixels only appear to somewhat overlap the more ambiguous inland RADAR channel ($\leq$1 km). I do not see any obvious correlation with the locations of the bright VIMS and RADAR channel pixels. The differences in the 5 μm I/F are unlikely to correspond with the width of a liquid stream or surface turbulence. Current estimates of apparent SAR channel widths are generally unreliable (Miller *et al.*, 2021). The I/F differences may simply result from the low signal-to-noise ratio at 5 μm (Sotin *et al.*, 2012). Comparing to the 2 km/pixel Amazon sunglint image in Figure 3.7, I can similarly identify sunglint from liquid surfaces but cannot deduce any information on the the type or shape of the liquid bodies. Thus, the observation of specular glint along the course

of the Apanohuaya Flumen suggests liquid is occupying the apparent channel. I also note a nearby channel with probable liquid fill ∼25 km to the north supported by a specular reflection in RADAR altimetry observations in Figure 3.6 (Poggiali *et al.*, 2018).

Remote-sensing sunglint observations of Earth's water-coated surfaces at twilight offer a terrestrial analog to the brightened liquid surfaces along the Punga Mare coastline. Figure 3.7 shows an astronaut photo of the Amazon River and its floodplains brightened by sunglint and observed at an oblique angle (>140°). The scene of dark, rough land surfaces and bright water bodies of the Amazon are analogous to the dark land and brightened liquid surfaces of the Punga Mare coastline. In the astronaut photo, I note differences in liquid surface brightness caused by cloud shadows and roughened surface flows. At 20 m/pixel, I can observe a fairly uniform brightness for the river channels and other liquid bodies. For a better comparison to the T110 observation, the Amazon sunglint image is downscaled to a similar spatial sampling in the bottom image of Figure 3.7. The main rivers and lakes are still detectable, but all the coastline features are lost. Darker portions of the Amazon River are harder to discern, possibly analogous to the dark VIMS pixels of Apanohuaya Flumen. Thus, the bright Apanohuaya pixels in the T110 observation may also be narrow liquid body features, albeit unresolved.

3.3.3 *Sun glitter*

The last anomalous specular feature within the land surfaces that I identify consists of brightened pixels that occur at the land-sea interface along Punga's eastern shoreline. I observe a thin pink-white strip along the central eastern coast of Punga Mare between the Apanohuaya river mouth and a peninsula (right panel, Figure 3.8). The brightened coast pixels appear in the inner portion of the sun glitter zone (specular deviation angles of 1.5-2.0°) with a restricted range of 5 μm I/F values (Figure 3.5A). Other documented instances of 5-μm-bright margins at fine spatial sampling include southern Ontario Lacus (Barnes *et al.*, 2009). At 5.0 μm, I see a notable I/F contrast between the land, sea, and brightened coastline pixels (Figure 3.8). However, there

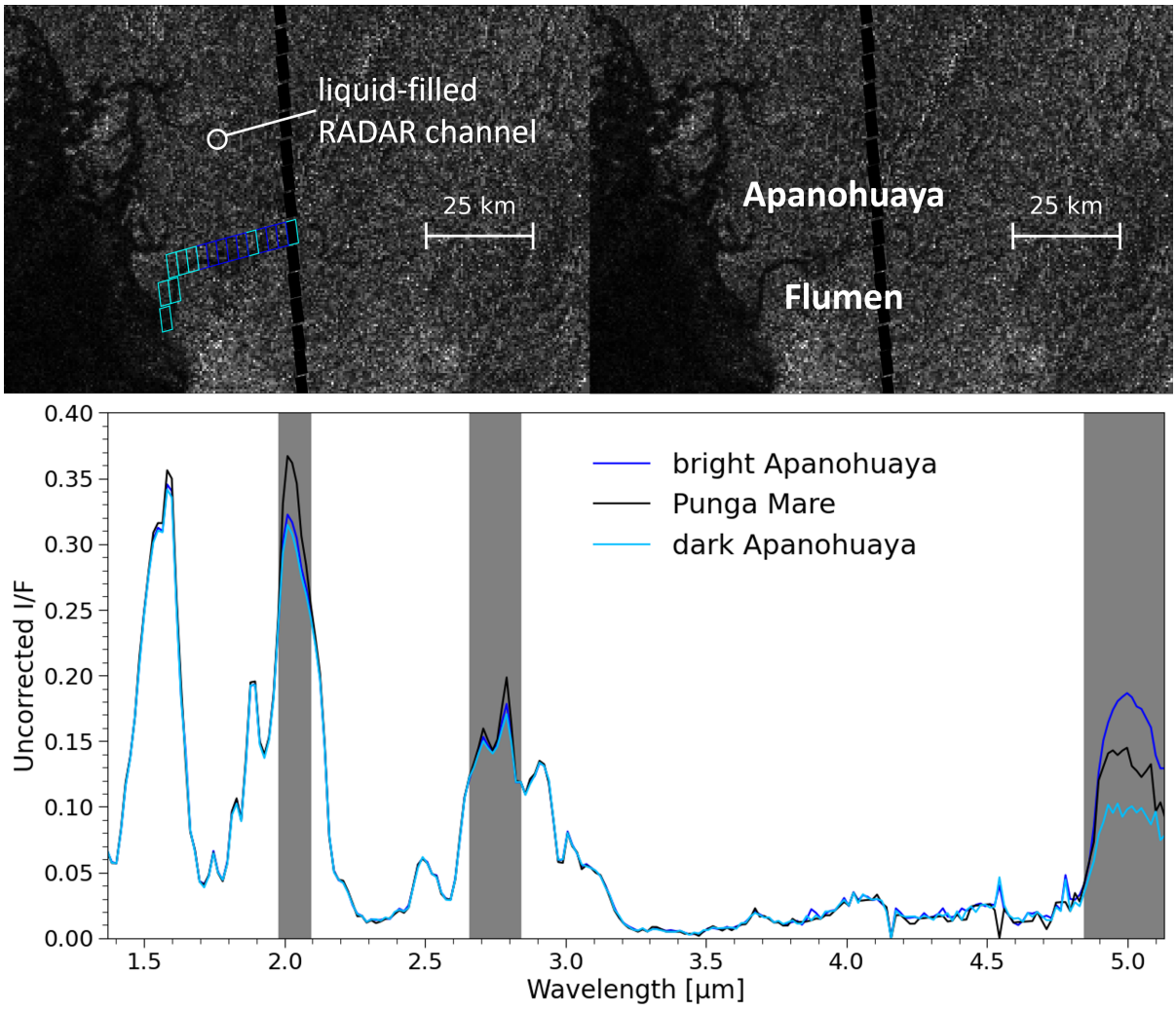

FIGURE 3.6: The top left panel shows a zoomed look of the T29 SAR swath over Apanohuaya Flumen. Bright and dark VIMS pixels projected over Apanohuaya Flumen are blue and sky blue respectively. The white circle denotes the location of a possible nearby liquid-filled channel detected by RADAR altimetry (Poggiali *et al.*, 2018). The top right panel shows the same SAR swath with a dark sinuous outline of Apanohuaya Flumen and a partial overlap with the locations of VIMS pixels up to 30 km inland from Punga Mare. The bottom panel shows the average spectra of bright and dark Apanohuaya pixels relative to a nearby Punga Mare pixel. Grey regions indicate surface windows with high atmospheric transparency.

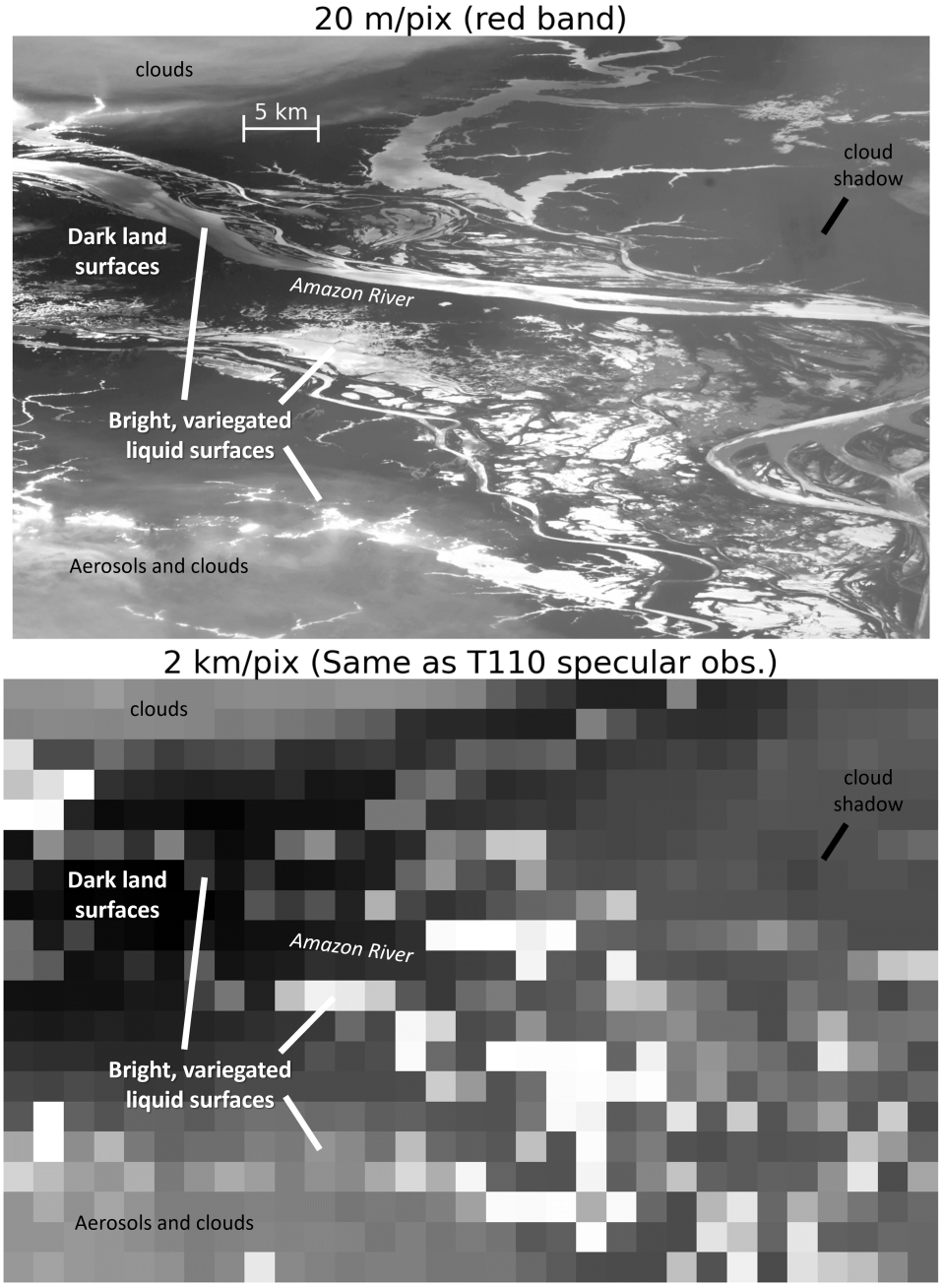

FIGURE 3.7: Top: The red band image from Astronaut Photo ISS017-E-13856 of twilight sunglint on the Amazonian floodplains at a high phase angle (>140°). The oblique viewing geometry reveals complex structures of the liquid surface features, including rivers, coastlines, and lakes. All rough land appears black. Haze scattering from local fire smoke and clouds are present in many parts of the photo. Cloud shadows visibly darken portions of land and liquid surfaces. Bottom: Same as Top image but downscaled to the spatial sampling of the T110 observation for direct comparison.

is no measurable 2.0 μm I/F signature for the brightened coasts, possibly owing to a surface coloration/absorption effect or the higher optical depth relative to the 5 μm window.

When the T110 Punga brightened coast pixels are projected onto the north polar RADAR map (Figure 3.2), the brightest pixels mostly overlap, primarily, the seaward side of the coast. Nonetheless, I include VIMS pixels from both sides of the eastern Punga coastline in our analysis. The offshore pixels are generally dimmer than the onshore pixels (Figure 3.5A) In this case, onshore pixels represent rough terrain adjacent to the Punga coastline. The offshore pixels represent some component of liquid surfaces from Punga Mare, but may include an interaction of liquid surfaces with the land terrain (e.g., waves on a beach). Thus, I require a further consideration of the environmental conditions of the air-sea-land interfaces of Punga Mare to deduce possible explanations for the 5 μm signature of the brightened coasts.

A consequence of brightened coastal seas may be spatially-variable surface wave conditions during the observation. In this first hypothesis, the sea surfaces in the nearshore zone near eastern Punga coastlines would be variegated wave fields of capillary waves. Further offshore, the sea surfaces would be nearly wave-free. A few local observations support the idea of persistent wave activity along the Punga coastlines. Numerous reports of north polar precipitation (Dhingra *et al.*, 2019, 2020) and large-scale cloud systems (Turtle *et al.*, 2018; Corlies *et al.*, 2020) suggest strong winds are present during transient periods of the summer. Wind speeds of 0.4-0.7 m s^{-1} are necessary to reach the capillary wave threshold in liquid methane (Hayes *et al.*, 2013). Limited amounts of capillary waves may develop from weak winds in the offshore zone (Toffoli and Bitner-Gregersen, 2017). In the nearshore zone, the shallow seafloor depths can allow for an increase in the height of those offshore capillary waves (i.e. wave shoaling) that can be detected as bright sun glitter (Strong and Ruff, 1970). Thus, the Punga brightened coasts may be interpreted as a narrow shoreline margin of rough sea surfaces while nearly flat sea surfaces are further offshore.

Along the southern coasts of Punga Mare, I note 4 small anomalously bright features inside various coastal inlets at 5 μm in Figure 3.5B. These "bright coastal

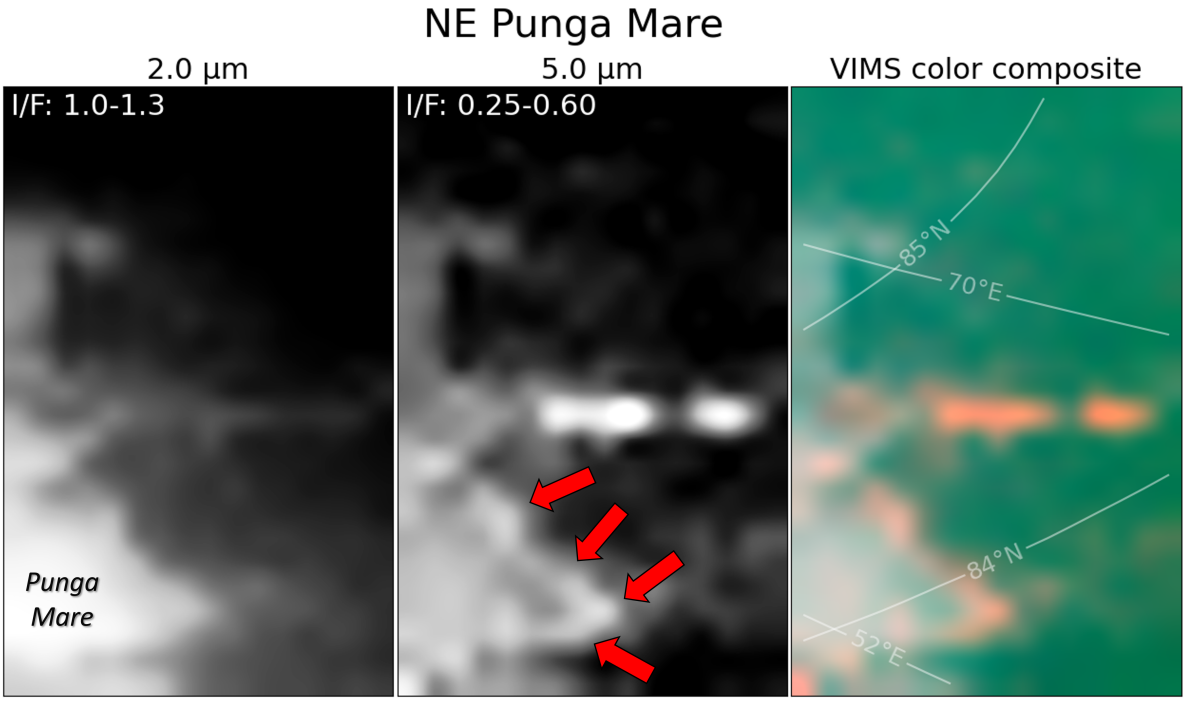

FIGURE 3.8: A row of images of brightened coastlines along northeastern Punga Mare. The images are taken at 2.0 µm, 5.0 µm, and the VIMS color scheme in Figure 3.1 in the left, center, and right panels respectively. Red arrows denote the brightened coasts by their thin structure at the land-sea interface in the 5.0 µm images. The top-left corners note the VIMS I/F range for each greyscale image. Translucent lines in the right panel are a superimposed geographic grid. Note that the brightened coasts appear between specular deviation angles of 1.5-2.0°.

inlet" pixels are likely roughened sea surfaces since they appear in the inner portion of the sun glitter zone at $\sim$2.5° in the top panel of Figure 3.5A. The large range of 5 μm I/F values for the green inlet pixels in Figure 3.5A suggest different surface roughnesses at each sea inlet. A polar projection of the brightened inlet pixels on the RADAR map in Figure 3.2 reveals that their locations might coincide with river debouches, defined as the location where narrow channels discharge into the broader bays (Sinus). In particular, a km-wide channel connects the inner basin and embayment of Avacha Sinus. Fagaloa, Saldanha, and Tumaco Sinus are likely associated with rias (i.e. flooded estuaries) due to the irregular and crenulated coastline shape, similar to the southern coasts of Ligeia Mare (Wasiak *et al.*, 2013).

For Avacha Sinus, the multiple bright pixels may indicate an active fluid flow that generates an extended region of rough sea surfaces at the channel constriction, known as a gut in coastal geomorphology. A gut is often associated with a fast tidal current, such as the Digby Gut in Canada (Karsten *et al.*, 2012). The geological set-up of Avacha Sinus appears to be more complex than the other sea inlets with its narrow interior channel separating a Punga embayment and a wide estuary. *Cassini* VIMS observations have found evidence for tidal currents in several narrow straits of Kraken-Ligeia Maria (Heslar *et al.*, 2020; Sotin *et al.*, 2015), but their hydraulic parameters remain unknown. However, the lake hydrology and high latitude of Punga Mare is unfavorable for large tides to exchange in coastal inlets (Tokano *et al.*, 2014; Vincent *et al.*, 2018).

An alternative explanation for the brightened VIMS pixels may be dinitrogen bubble exsolution events, which is supported by experimental (Malaska *et al.*, 2017) and remote sensing observations (Hofgartner *et al.*, 2014). The main constituent of Titan's atmosphere, dinitrogen, has a high solubility of 5-20 mol% in liquid methane-ethane mixtures (Hartwig *et al.*, 2018), which is 1000 times greater than carbon dioxide in terrestrial seas (Al-Anezi *et al.*, 2008). Bubble effervescence is a prospective scenario for pluvial methane runoff entering a hydrocarbon sea with a small ethane concentration ($\geq$5%) or a thermal anomaly ($\geq$2 K) at river debouches (Farnsworth *et al.*, 2019; Malaska *et al.*, 2017). A stratified sea with a methane-rich epilimnion

(surface layer) and ethane-rich hypolimnion (bottom layer) could be more favorable for bubble exsolution. However, even small currents with flow velocities of 1 cm s^1 on the sea surface, caused by tides or winds, would likely result in fully turbulent mixing (i.e. Reynolds number of $\sim 10^9$ for a 100 m deep lake) and destroy any stratification (Steckloff *et al.*, 2020).

Alternatively, a thermal anomaly of $\geq$2 K can occur, considering rain drops can reach the surface below the ambient air temperature due to evaporative cooling as supported by physical models of rainfall on Titan (Graves *et al.*, 2008) and CIRS surface temperature measurements (Dhingra *et al.*, 2021). However, the evolution of the temperature profile for a methane streamflow along its river course is unknown and remains open for future research. Altogether, the thermal conditions and river-sea compositions expected for the summer environment of Punga Mare are favorable for bubble exsolution at debouches, but unanswered questions still linger.

There are also two instances of sun glitter in VIMS' T110 observations: 1) adjoined to the largest island of Hawaiki Insulae and 2) offshore from the central southern Punga coastlines, which are displayed as orange pixels in Figure 3.2. Their high 5 μm I/F values in Figure 3.5A is consistent with previous sun glitter observations (Heslar *et al.*, 2020). The islands of Hawaiki Insulae are an isolated archipelago. The brightest Hawaiki sun glitter cluster on the north side of the largest island, suggesting a build-up of rougher seas. I note the Hawaiki sun glitter pixels directly overlay the islands in RADAR in Figure 3.2 likely due to poor signal-to-noise at 5 μm. I confirm the detection of the two larger islands in the 2 μm window in Figure 3.4. The single pixel of offshore sun glitter indicates rough sea surfaces are not necessarily restricted to the nearshore zones. The sun glitter observations support the presence of local-scale (1-10 km) surface circulation patterns in Punga Mare in the summertime.

The variable specular glint in Fundy Sinus and isolated sun glitter observations indicate a widespread occurrence of variegated sea surfaces across different environments of Punga Mare. The apparently random geographic distribution of calm seas in Fundy Sinus does not point to a strong topographic or bathymetric control of the sea surface roughness. Rather, there is likely an intricate interplay of air-sea

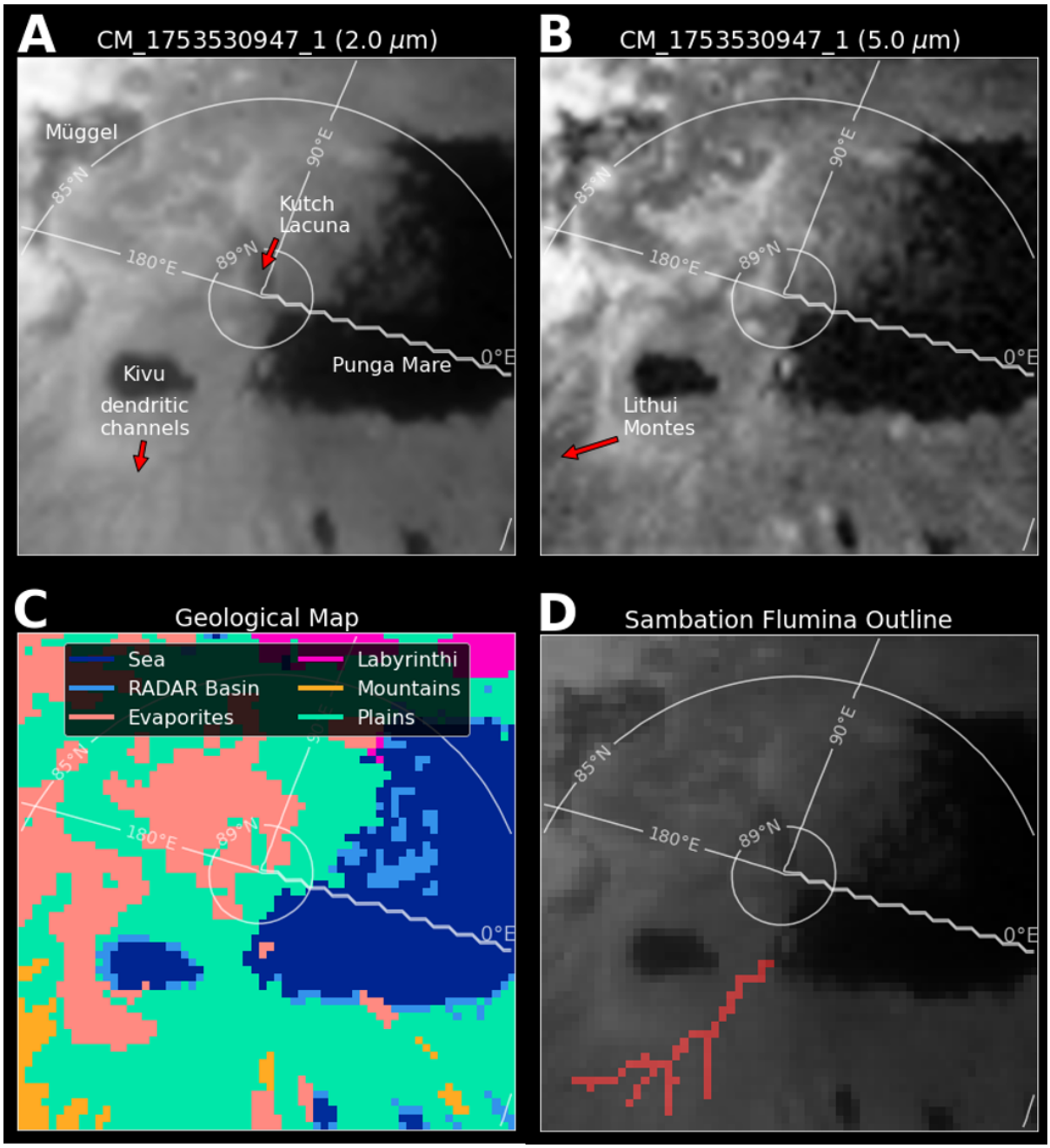

FIGURE 3.9: A) Unprojected T93 VIMS observation CM_1753530947_1 at 2 μm with a geographic grid and geographic features labelled. Note the dark "dendritic channels" that link Lithui Montes to Punga Mare. B) Same as A, but at 5 μm. Lithui Montes shows evidence of water-ice enrichment by the dark 5-um signal. The channels are not very observable due to a low 5 μm signal-to-noise ratio. C) Global Titan geological map (Lopes *et al.*, 2019b) and evaporite (MacKenzie *et al.*, 2014) units assigned to unprojected cube CM_1753530947_1. D) Pixelated image of A with the red outline of the Sambation Flumina channels.

interactions with local island topography. Atmospheric models and high-sampling cloud observations also support an orographic influence of cloud development and near-surface winds on Titan (Barth, 2010).

Depending on the wind direction, the potential island topographic peaks may act to redirect the predominant winds and create a leeward wind shadow. This phenomenon may explain the smooth seas interspersed with roughened seas in eastern Fundy Sinus and Tumaco Sinus. Meanwhile, the Hawaiki sun glitter may identify the generation of surface waves in coastal zones on the windward coasts of islands. Geomorphologic analysis suggests a topographic relief of few hundred meters for Hawaiki Insulae (Birch *et al.*, 2017), which may allow for the development of a wind shadow. Future specular observations from a Titan orbiter may decipher wind shadows that are commonplace in sunglint observations of equatorial archipelagos on Earth, such as the Canary Islands (Fett and Rabe, 1975).

Isolated patches of wind-roughened seas can occur anywhere on a lake surface. In northern summer, the high latitude of Punga Mare allows for a continuous insolation that drives a permanent planetary boundary layer (Roe, 2012). Thus, I can reasonably expect turbulent weather, which would drive ample opportunity for surface wind developments over Punga Mare. This scenario of localized wind-roughened sea surfaces is common for a windy day over a terrestrial lake and supported by prior evidence of sun glitter on Punga Mare in northern spring (Barnes *et al.*, 2014).

CHAPTER 4

Conclusion[4]

The T104 and T105 VIMS observations show evidence of isolated sun glitter across the surface of Kraken Mare at moderate sampling (17-21 km/pixel) that indicate surface waves. Fine-sampling observations (<10 km/pixel) during the same flybys find evidence of variegated wave fields and confirm the moderate-sampling sun glitter over three narrow straits: Bayta Fretum, Seldon Fretum, and Tunu Sinus. Geographic projection of the VIMS observations and spectral analysis indicate that the sun glitter is confined to the sea surfaces and distinct from other known surface and atmospheric features, namely clouds/fog, potential rain-wetted surfaces, and evaporites.

Fine-sampling sun glitter imagery from the T104 flyby reveals an extended set of wave fields that are parallel with the Bayta Fretum shorelines. While an arrow cloud and Ligeia surface waves observed during T104 provide evidence for convective weather, we cannot determine if storm-induced winds are solely responsible for the Bayta waves. Overall, our observations suggest complex influences for wave activity in Bayta Fretum, possibly originating from the winds. The tidal currents in Bayta Fretum are unlikely to reach the capillary-gravity wave generation threshold. Overall, we cannot be certain of tidal or wind wave action in Bayta Fretum without knowledge of its bathymetry.

We observe several instances of sun glitter in the Seldon Fretum region in two T105 fine-sampling VIMS observations. In particular, Seldon Fretum and the entrance of Lulworth Sinus host the brightest sun glitter, which we attribute to the constriction of northward tidal currents predicted by tidal models (Tokano *et al.*, 2014, Vincent *et al.*, 2018) for a true anomaly of 246° (Table 3.1). The T105 Hufaidh and Bermoothes Insulae sun glitter suggest a complex interaction of wind and tidal activity. However,

[4]Significant portions of this chapter are taken from the following references:
Heslar *et al*. (2020): "Heslar M.F., Barnes J.W., Soderblom J.M., Seignovert B., Dhingra R.D., and Sotin C. 2020. Tidal Currents Detected in Kraken Mare Straits from Cassini VIMS Sun Glitter Observations. *Planetary Science Journal* 1:35."
Heslar M.F. & Barnes J.W. 2022 *Planetary Science Journal*. (under review)

one instance of sun glitter ∼30 km offshore from Bermoothes Insula may indicate a detection of wind seas over Kraken Mare during the T105 flyby or an anomalous feature underneath the sea surface that interrupts surface currents. Internal waves are an unlikely prospect for a Seldon Fretum with shallow bathymetry.

We infer about the coastal morphology of Hufaidh and Bermoothes Insulae from the T105 Seldon wave observations. The Torres Strait and the Åland region may serve as analogous features to Hufaidh and Bermoothes Insulae, considering they are both shallow straits with many islands that experience complex surface circulation and wave patterns. However, there is a notable difference in their marine environments as the Torres Strait hosts an abundant sediment supply from Papua New Guinea rivers with unique seafloor bedforms (e.g. sandbars) formed by tidal action. Hufaidh and Bermoothes Insulae could have submarine sedimentary features, such as "icy" sandbars. Alternatively, Hufaidh and Bermoothes Insulae may simply host a mix of cliffed and ria coastlines with no major sedimentary deposits, just like the Åland region. Also, the islands of Hufaidh and Bermoothes Insulae are likely isolated peaks of the primordial Titan crust due to either the drowning of local peaks from a period of sea level rise or local tectonic uplift. These scenarios match the geological origins of the Torres Strait and the Åland region respectively. Finally, the shorelines of Bermoothes Insula and Lulworth Sinus may show evidence of a submergent coastline with flooded river valleys or rias and imply a recent episode of sea-level rise for Kraken Mare. Tunu Sinus tidal flows and the common equipotential surface of Titan's Maria may lean evidence toward a surface hydrological connection via unresolved rivers between Kraken and Punga Maria.

The VIMS T110 observation highlights a diverse range of oceanographic and coastal phenomena on the surface of Punga Mare. The location of specular features relative to the specular and sun glitter zones plays a crucial role in determining their physical origin and surface roughness. The high phase of the T110 observation helps constrain the origin of specular features to the direct air-sea-land interface. Observation geometry, geographical context, and the relative pixel fill fraction of the

land and liquid surfaces all provide useful insights into the physical origin of each specular feature.

We document new evidence for a liquid-filled channel in Apanohuaya Flumen. Other specular reflections in RADAR altimetry observations detected at limited points within channels near Ligeia and Punga Mare suggest the presence of smooth liquid surfaces (Poggiali *et al.*, 2016, 2018). The new Apanohuaya VIMS glint observation provide further evidence that liquids are present along the entire course of apparent SAR channels. An elevated region with $\sim$1 km of relief separating Ligeia and Punga Mare (Birch *et al.*, 2017) also indicates Apanohuaya Flumen is likely a downstream river, consistent with other rivers like Vid Flumina (Poggiali *et al.*, 2016). A similar geological setup of elevated channels is present with Lithui Montes and Sambation Flumina feeding into northwest Punga Mare (Figure 3.9). Altogether, the various observations of liquid-filled channels support the presence of unique drainage basins for each northern sea driven by an active hydrological cycle of liquid methane. This scenario mirrors proposed drainage basins in the southern hemisphere (Birch *et al.*, 2018; Dhingra *et al.*, 2018).

The variety of sun glitter features observed in the T110 observation tells a story of a dynamic surface environment on Punga Mare in summer. Anomalous margins along shorelines suggest air-sea-land interactions potentially driven by summer winds. Along the eastern Punga coast, surface winds may create a coastal margin of rough seas with capillary waves juxtaposed to nearly smooth sea surfaces in the offshore zone. Fundy specular glint and sun glitter, both near islands and away from coastlines, strongly indicate direct air-sea interactions with wind. With the onset of northern summer from 2012-2015, there were many similar occurrences of possible wind-roughened sea surfaces. Such reports include roughened seas scattered on Punga (Barnes *et al.*, 2014), linear wave fields along the west Kraken coast (Heslar *et al.*, 2020), and RADAR-bright "magic islands" in two locations of Ligeia (Hofgartner *et al.*, 2016). Overall, the various instances of wind-roughened sea surfaces are independent of the relative location within the seas (e.g. coastline vs offshore) that mirrors wind-wave observations on Earth (Toffoli and Bitner-Gregersen, 2017).

Nonetheless, some T110 sun glitter features and formerly reported sea surface anomalies are constrained to the ria coastlines of the northern seas. Brightened 5 μm pixels at the transition point between rivers and bays (debouches) in southern Punga coastal inlets imply fluid exchanges. At Avacha Sinus, tidal exchanges may be occurring in a narrow strait that connects Punga Mare and a wide estuary. Another plausible interaction at debouches may be nitrogen bubble outburst events from a methane-nitrogen river. The bubble outburst hypothesis may be supported by a report of anomalous RADAR altimeter signals in a coastal region of Moray Sinus in Kraken during the T104 flyby (Poggiali *et al.*, 2020). Similarly, the Moray anomaly could result from sea surfaces roughened by winds or bubble exsolution from methane-nitrogen streamflow (Poggiali *et al.*, 2020). Based on these observations, I suggest that there is intriguing small-scale (sub-km) phenomena within Titan's seas and along the shorelines deserving further exploration.

Bibliography

Al-Anezi K., Somerfield C., Mee D., and Hilal N. 2008. Parameters affecting the solubility of carbon dioxide in seawater at the conditions encountered in msf desalination plants. Desalination 222:548–571.

Barnes J.W., Bow J., Schwartz J., Brown R.H., Soderblom J.M., Hayes A.G., Vixie G., Le Mouélic S., Rodriguez S., Sotin C., *et al*. 2011a. Organic sedimentary deposits in titan's dry lakebeds: Probable evaporite. Icarus 216:136–140.

Barnes J.W., Brown R.H., Soderblom J.M., Soderblom L.A., Jaumann R., Jackson B., Le Mouélic S., Sotin C., Buratti B.J., Pitman K.M., *et al*. 2009. Shoreline features of titan's ontario lacus from cassini/vims observations. Icarus 201:217–225.

Barnes J.W., Brown R.H., Soderblom L., Sotin C., Le Mouèlic S., Rodriguez S., Jaumann R., Beyer R.A., Buratti B.J., Pitman K., *et al*. 2008. Spectroscopy, morphometry, and photoclinometry of titan's dunefields from cassini/vims. Icarus 195:400–414.

Barnes J.W., Buratti B.J., Turtle E.P., Bow J., Dalba P.A., Perry J., Brown R.H., Rodriguez S., Le Mouélic S., Baines K.H., *et al*. 2013a. Precipitation-induced surface brightenings seen on titan by cassini vims and iss. Planetary Science 2:1.

Barnes J.W., Clark R.N., Sotin C., Ádámkovics M., Appéré T., Rodriguez S., Soderblom J.M., Brown R.H., Buratti B.J., Baines K.H., *et al*. 2013b. A transmission spectrum of titan's north polar atmosphere from a specular reflection of the sun. The Astrophysical Journal 777:161.

Barnes J.W., Soderblom J.M., Brown R.H., Soderblom L.A., Stephan K., Jaumann R., Le Mouélic S., Rodriguez S., Sotin C., Buratti B.J., *et al*. 2011b. Wave constraints for titan's jingpo lacus and kraken mare from vims specular reflection lightcurves. Icarus 211:722–731.

Barnes J.W., Sotin C., Soderblom J.M., Brown R.H., Hayes A.G., Donelan M., Rodriguez S., Le Mouélic S., Baines K.H., and McCord T.B. 2014. Cassini/vims observes rough surfaces on titan's punga mare in specular reflection. Planetary Science 3:3.

Barth E.L. 2010. Cloud formation along mountain ridges on titan. Planetary and Space Science 58:1740–1747.

Birch S., Hayes A., Corlies P., Stofan E., Hofgartner J., Lopes R., Lorenz R., Lunine J., MacKenzie S., Malaska M., *et al*. 2018. Morphological evidence that titan's southern hemisphere basins are paleoseas. Icarus 310:140–148.

Birch S., Hayes A., Dietrich W., Howard A., Bristow C., Malaska M., Moore J., Mastrogiuseppe M., Hofgartner J., Williams D., *et al*. 2017. Geomorphologic mapping of titan's polar terrains: Constraining surface processes and landscape evolution. Icarus 282:214–236.

Bird E.C. 2011. Coastal geomorphology: an introduction. John Wiley & Sons.

Bréon F. and Henriot N. 2006. Spaceborne observations of ocean glint reflectance and modeling of wave slope distributions. Journal of Geophysical Research: Oceans 111.

Brown M., Smith A., Chen C., and Ádámkovics M. 2009. Discovery of fog at the south pole of titan. The Astrophysical Journal 706:L110.

Brown R.H., Baines K.H., Bellucci G., Bibring J.P., Buratti B.J., Capaccioni F., Cerroni P., Clark R.N., Coradini A., Cruikshank D.P., *et al*. 2004. The cassini visual and infrared mapping spectrometer (vims) investigation. Space Science Reviews 115:111–168.

Burr D.M., Drummond S.A., Cartwright R., Black B.A., and Perron J.T. 2013. Morphology of fluvial networks on titan: Evidence for structural control. Icarus 226:742–759.

Burr D.M., Emery J.P., Lorenz R.D., Collins G.C., and Carling P.A. 2006. Sediment transport by liquid surficial flow: Application to titan. Icarus 181:235–242.

Charnay B., Barth E., Rafkin S., Narteau C., Lebonnois S., Rodriguez S., Courrech du Pont S., and Lucas A. 2015. Methane storms as a driver of titan's dune orientation. Nature Geoscience 8:362–366.

Chatain A., Rafkin S.C., Soto A., Hueso R., and Spiga A. 2022. Air–sea interactions on titan: Effect of radiative transfer on the lake evaporation and atmospheric circulation. The Planetary Science Journal 3:232.

Cordier D., García-Sánchez F., Justo-García D.N., and Liger-Belair G. 2017. Bubble streams in titan's seas as a product of liquid n2+ ch4+ c2h6 cryogenic mixture. Nature Astronomy 1:1–4.

Corlies P., Hayes A., Adamkovics M., Rodriguez S., Turtle E., Rojo P., Lora J., Mitchell J., Lunine J., Soderblom J., *et al*. 2020. Updates on the titan cloud monitoring campaign: Large storms and future forecasts. *In* AAS/Division for Planetary Sciences Meeting Abstracts, vol. 52, pages 411–06.

Cox C. and Munk W. 1954. Measurement of the roughness of the sea surface from photographs of the sun's glitter. Josa 44:838–850.

Craik A.D. *et al*. 2004. The origins of water wave theory. Annual review of fluid mechanics 36:1–28.

Daniell J.J. 2015. Bedform facies in western torres strait and the influence of hydrodynamics, coastal geometry, and sediment supply on their distribution. Geomorphology 235:118–129.

Dhingra R.D., Barnes J.W., Brown R.H., Burrati B.J., Sotin C., Nicholson P.D., Baines K.H., Clark R.N., Soderblom J.M., Jauman R., *et al*. 2019. Observational evidence for summer rainfall at titan's north pole. Geophysical Research Letters 46:1205–1212.

Dhingra R.D., Barnes J.W., Heslar M.F., Brown R.H., Buratti B.J., Sotin C., Soderblom J.M., Rodriguez S., Le Mouélic S., Nicholson P.D., *et al*. 2020. Spatio-temporal variation of bright ephemeral features on titan's north pole. The Planetary Science Journal 1:31.

Dhingra R.D., Barnes J.W., Yanites B.J., and Kirk R.L. 2018. Large catchment area recharges titan's ontario lacus. Icarus 299:331–338.

Dhingra R.D., Jennings D.E., Barnes J.W., and Cottini V. 2021. Lower surface temperature at bright ephemeral feature site on titan's north pole. Geophysical Research Letters page e2020GL091708.

Dronkers J. 2005. Dynamics of coastal systems, vol. 25. World Scientific.

Edelman N. and Jaanus M. 1980. Stratigraphy and plate tectonics in the archipelago of southwestern finland. Geologiska Föreningen i Stockholm Förhandlingar 102:187–187.

Erkkilä A. and Kalliola R. 2004. Patterns and dynamics of coastal waters in multi-temporal satellite images: support to water quality monitoring in the archipelago sea, finland. Estuarine, Coastal and Shelf Science 60:165–177.

Ermakov S.A., Danilicheva O.A., Kapustin I.A., and Molkov A.A. 2019. Drift and shape of oil slicks on the water surface. *In* Remote Sensing of the Ocean, Sea Ice, Coastal Waters, and Large Water Regions 2019, vol. 11150, page 111500J, International Society for Optics and Photonics.

Farnsworth K.K., Chevrier V.F., Steckloff J.K., Laxton D., Singh S., Soto A., and Soderblom J.M. 2019. Nitrogen exsolution and bubble formation in titan's lakes. Geophysical Research Letters 46:13658–13667.

Fett R.W. and Rabe K. 1975. Island barrier effects on sea state and atmospheric moisture as detected by a numerical wave model and sensors of the defense meteorological satellite program (dmsp). Tech. rep., ENVIRONMENTAL PREDICTION RESEARCH FACILITY (NAVY) MONTEREY CALIF.

Flasar F., Achterberg R., Conrath B., Gierasch P., Kunde V., Nixon C., Bjoraker G., Jennings D., Romani P., Simon-Miller A., *et al*. 2005. Titan's atmospheric temperatures, winds, and composition. Science 308:975–978.

Ghafoor N.A.L., Zarnecki J.C., Challenor P., and Srokosz M.A. 2000. Wind-driven surface waves on titan. Journal of Geophysical Research: Planets 105:12077–12091.

Glover I. 1977. Sunda and sahul—prehistoric studies in southeast asia, melanesia and australia: Edited by j. allen, j. golson and r. jones. 1977. 647 pp. 84 figures and plates. london: Academic press.£ 12· 50.

Graves S., McKay C., Griffith C., Ferri F., and Fulchignoni M. 2008. Rain and hail can reach the surface of titan. Planetary and Space Science 56:346–357.

Griffith C.A., Hall J.L., and Geballe T.R. 2000. Detection of daily clouds on titan. Science 290:509–513.

Grima C., Mastrogiuseppe M., Hayes A.G., Wall S.D., Lorenz R.D., Hofgartner J.D., Stiles B., Elachi C., Team C.R., *et al*. 2017. Surface roughness of titan's hydrocarbon seas. Earth and Planetary Science Letters 474:20–24.

Hanley J., Groven J.J., Grundy W., Pearce L.A., Dustrud S., Lindberg G.E., and Tegler S.C. 2018. Characterization of possible two liquid layers in titan seas. *In* AAS/Division for Planetary Sciences Meeting Abstracts# 50, vol. 50, pages 203–10.

Harris P.T. 1988. Sediments, bedforms and bedload transport pathways on the continental shelf adjacent to torres strait, australia—papua new guinea. Continental Shelf Research 8:979–1003.

Hartwig J., Meyerhofer P., Lorenz R., and Lemmon E. 2018. An analytical solubility model for nitrogen–methane–ethane ternary mixtures. Icarus 299:175–186.

Hayes A., Aharonson O., Lunine J., Kirk R., Zebker H., Wye L., Lorenz R., Turtle E., Paillou P., Mitri G., *et al*. 2011. Transient surface liquid in titan's polar regions from cassini. Icarus 211:655–671.

Hayes A.G. 2016. The lakes and seas of titan. Annual Review of Earth and Planetary Sciences 44:57–83.

Hayes A.G., Birch S., Dietrich W.E., Howard A.D., Kirk R.L., Poggiali V., Mastrogiuseppe M., Michaelides R., Corlies P., Moore J., *et al*. 2017. Topographic constraints on the evolution and connectivity of titan's lacustrine basins. Geophysical Research Letters 44:11–745.

Hayes A.G., Lorenz R.D., Donelan M., Manga M., Lunine J., Schneider T., Lamb M., Mitchell J., Fischer W., Graves S., *et al*. 2013. Wind driven capillary-gravity waves on titan's lakes: Hard to detect or non-existent? Icarus 225:403–412.

Hayes A.G., Lorenz R.D., and Lunine J.I. 2018. A post-cassini view of titan's methane-based hydrologic cycle. Nature Geoscience 11:306–313.

Hemer M., Harris P., Coleman R., and Hunter J. 2004. Sediment mobility due to currents and waves in the torres strait–gulf of papua region. Continental Shelf Research 24:2297–2316.

Heslar M.F., Barnes J.W., Soderblom J.M., Seignovert B., Dhingra R.D., and Sotin C. 2020. Tidal currents detected in kraken mare straits from cassini vims sun glitter observations. The Planetary Science Journal 1:35.

Hofgartner J., Hayes A.G., Lunine J., Zebker H., Stiles B., Sotin C., Barnes J.W., Turtle E.P., Baines K., Brown R.H., *et al*. 2014. Transient features in a titan sea. Nature Geoscience 7:493–496.

Hofgartner J.D., Hayes A.G., Lunine J.I., Zebker H., Lorenz R.D., Malaska M.J., Mastrogiuseppe M., Notarnicola C., and Soderblom J.M. 2016. Titan's "magic islands": Transient features in a hydrocarbon sea. Icarus 271:338–349.

Jackson C. 2007. Internal wave detection using the moderate resolution imaging spectroradiometer (modis). Journal of Geophysical Research: Oceans 112.

Jackson C.R. and Alpers W. 2010. The role of the critical angle in brightness reversals on sunglint images of the sea surface. Journal of Geophysical Research: Oceans 115.

Kahma K., Pettersson H., and Tuomi L. 2003. Scatter diagram wave statistics from the northern baltic sea. MERI–Report Series of the Finnish Institute of Marine Research 49:15–32.

Karkoschka E., McEwen A., and Perry J. 2017. Creating the best global mosaic of titan's surface albedo using cassini images. *In* AAS/Division for Planetary Sciences Meeting Abstracts# 49, vol. 49, pages 301–06.

Karsten R., O'Flaherty-Sproul M., McMillan J., Culina J., Trowse G., and Hay A. 2012. Analysis of tidal turbine arrays in digby gut and petit passage, nova scotia. *In* Proceedings of the 4th International Conference on Ocean Energy.

Kay S., Hedley J.D., and Lavender S. 2009. Sun glint correction of high and low spatial resolution images of aquatic scenes: A review of methods for visible and near-infrared wavelengths. Remote sensing 1:697–730.

Kudryavtsev V., Yurovskaya M., Chapron B., Collard F., and Donlon C. 2017. Sun glitter imagery of surface waves. part 2: Waves transformation on ocean currents. Journal of Geophysical Research: Oceans 122:1384–1399.

Lawrey E. 2013. Torres strait clear sky, clear water landsat composite (nerp te 13.1 eatlas, aims, source: Nasa),[datafile]. eatlas, aims [producer]. cc by 3.0 au [license].

Le Mouélic S., Cornet T., Rodriguez S., Sotin C., Seignovert B., Barnes J.W., Brown R.H., Baines K.H., Buratti B.J., Clark R.N., *et al*. 2019a. The cassini vims archive of titan: From browse products to global infrared color maps. Icarus 319:121–132.

Le Mouélic S., Cornet T., Rodriguez S., Sotin C., Seignovert B., Barnes J.W., Brown R.H., Baines K.H., Buratti B.J., Clark R.N., *et al*. 2019b. The cassini vims archive of titan: From browse products to global infrared color maps. Icarus 319:121–132.

Lemckert C., Zier J., and Gustafson J. 2009. Tides in torres strait. Journal of Coastal Research pages 524–528.

Lindal G.F., Wood G., Hotz H., Sweetnam D., Eshleman V., and Tyler G. 1983. The atmosphere of titan: An analysis of the voyager 1 radio occultation measurements. Icarus 53:348–363.

Lopes R., Wall S., Elachi C., Birch S.P., Corlies P., Coustenis A., Hayes A., Hofgartner J., Janssen M.A., Kirk R., *et al*. 2019a. Titan as revealed by the cassini radar. Space Science Reviews 215:1–50.

Lopes R.M., Malaska M.J., Schoenfeld A.M., Solomonidou A., Birch S., Florence M., Hayes A., Williams D., Radebaugh J., Verlander T., *et al*. 2019b. A global geomorphologic map of saturn's moon titan. Nature Astronomy 4:228–233.

Lorenz R. 2003. The glitter of distant seas. Science 302:403–404.

Lorenz R. and Mitton J. 2010. Titan unveiled. *In* Titan Unveiled, Princeton University Press.

Lorenz R.D. 2013. Oceanography on saturn's moon, titan. *In* 2013 OCEANS-San Diego, pages 1–7, IEEE.

Lorenz R.D. 2014. The flushing of ligeia: Composition variations across titan's seas in a simple hydrological model. Geophysical Research Letters 41:5764–5770.

Lorenz R.D. and Hayes A.G. 2012. The growth of wind-waves in titan's hydrocarbon seas. Icarus 219:468–475.

Lorenz R.D., Kirk R.L., Hayes A.G., Anderson Y.Z., Lunine J.I., Tokano T., Turtle E.P., Malaska M.J., Soderblom J.M., Lucas A., *et al*. 2014. A radar map of titan seas: Tidal dissipation and ocean mixing through the throat of kraken. Icarus 237:9–15.

Lorenz R.D., Kraal E., Asphaug E., and Thomson R.E. 2003. The seas of titan. Eos, Transactions American Geophysical Union 84:125–132.

Lorenz R.D., Kraal E.R., Eddlemon E.E., Cheney J., and Greeley R. 2005. Sea-surface wave growth under extraterrestrial atmospheres: Preliminary wind tunnel experiments with application to mars and titan. Icarus 175:556–560.

Lorenz R.D., Tokano T., and Newman C.E. 2012. Winds and tides of ligeia mare, with application to the drift of the proposed time time (titan mare explorer) capsule. Planetary and Space Science 60:72–85.

Lothon M., Campistron B., Chong M., Couvreux F., Guichard F., Rio C., and Williams E. 2011. Life cycle of a mesoscale circular gust front observed by a c-band doppler radar in west africa. Monthly weather review 139:1370–1388.

Lucas A., Aharonson O., Deledalle C., Hayes A.G., Kirk R., and Howington-Kraus E. 2014. Insights into titan's geology and hydrology based on enhanced image processing of cassini radar data. Journal of Geophysical Research: Planets 119:2149–2166.

Lunine J.I. and Atreya S.K. 2008. The methane cycle on titan. Nature Geoscience 1:159–164.

Lynch D.K., Livingston W.C., and Livingston W. 2001. Color and light in nature. Cambridge University Press.

MacKenzie S. and Barnes J.W. 2016. Compositional similarities and distinctions between titan's evaporitic terrains. The Astrophysical Journal 821:17.

MacKenzie S.M., Barnes J.W., Sotin C., Soderblom J.M., Le Mouélic S., Rodriguez S., Baines K.H., Buratti B.J., Clark R.N., Nicholson P.D., *et al*. 2014. Evidence of titan's climate history from evaporite distribution. Icarus 243:191–207.

Malaska M.J., Hodyss R., Lunine J.I., Hayes A.G., Hofgartner J.D., Hollyday G., and Lorenz R.D. 2017. Laboratory measurements of nitrogen dissolution in titan lake fluids. Icarus 289:94–105.

Malaska M.J., Radebaugh J., Lopes R.M., Mitchell K.L., Verlander T., Schoenfeld A.M., Florence M.M., Le Gall A., Solomonidou A., Hayes A.G., *et al*. 2020. Labyrinth terrain on titan. Icarus page 113764.

Marouf E.A., French R.G., Wong K., Anabtawi A., Schinder P.J., *et al*. 2016. The calm methane northern seas of titan from cassini radio science observations. *In* AAS/Division for Planetary Sciences Meeting Abstracts# 48, vol. 48, pages 412–02.

Martonchik J.V. and Orton G.S. 1994. Optical constants of liquid and solid methane. Applied optics 33:8306–8317.

Mastrogiuseppe M., Poggiali V., Hayes A., Lunine J., Seu R., Di Achille G., and Lorenz R. 2018. Cassini radar observation of punga mare and environs: Bathymetry and composition. Earth and Planetary Science Letters 496:89–95.

Miller J., Birch S., Hayes A., Malaska M., Lopes R., Schoenfeld A., Corlies P., Burr D., Farr T., and Perron J. 2021. Fluvial features on titan and earth: Lessons from planform images in low-resolution sar. The Planetary Science Journal 2:142.

Mitchell J.L. and Lora J.M. 2016. The climate of titan. Annual Review of Earth and Planetary Sciences 44:353–380.

Mitri G., Showman A.P., Lunine J.I., and Lorenz R.D. 2007. Hydrocarbon lakes on titan. Icarus 186:385–394.

Munk W., Armi L., Fischer K., and Zachariasen F. 2000. Spirals on the sea. Proceedings of the Royal Society of London. Series A: Mathematical, Physical and Engineering Sciences 456:1217–1280.

Nappo C.J. 2013. An introduction to atmospheric gravity waves. Academic press.

Ori G.G., Marinangeli L., Baliva A., Bressan M., and Strom R.G. 1998. Fluid dynamics of liquids on titans surface. Planetary and space science 46:1417–1421.

Pilkey O.H., Neal W.J., Cooper J.A.G., and Kelley J.T. 2011. The world's beaches: a global guide to the science of the shoreline. Univ of California Press.

Poggiali V., Hayes A., Lunine J., Birch S., Mastrogiuseppe M., and Di Achille G. 2018. Canyons on titan: New insights by the cassini radar altimeter. 42nd COSPAR Scientific Assembly pages B5–3.

Poggiali V., Hayes A.G., Mastrogiuseppe M., Le Gall A., Lalich D., Gómez-Leal I., and Lunine J. 2020. The bathymetry of moray sinus at titan's kraken mare. Journal of Geophysical Research: Planets page e2020JE006558.

Poggiali V., Mastrogiuseppe M., Hayes A., Seu R., Birch S., Lorenz R., Grima C., and Hofgartner J. 2016. Liquid-filled canyons on titan. Geophysical Research Letters 43:7887–7894.

Rafkin S.C. and Barth E. 2015. Environmental control of deep convective clouds on titan: The combined effect of cape and wind shear on storm dynamics, morphology, and lifetime. Journal of Geophysical Research: Planets 120:739–759.

Rodriguez S., Le Mouélic S., Rannou P., Sotin C., Brown R., Barnes J., Griffith C., Burgalat J., Baines K., Buratti B., *et al*. 2011. Titan's cloud seasonal activity from winter to spring with cassini/vims. Icarus 216:89–110.

Roe H.G. 2012. Titan's methane weather. Annual Review of Earth and Planetary Sciences 40:355–382.

Seignovert B., Sotin C., Lawrence K.J., and Heslar M. 2020. Mapping vims specular reflections on titan's surface during the cassini mission. Tech. rep., Copernicus Meetings.

Soderblom J.M., Barnes J.W., Soderblom L.A., Brown R.H., Griffith C.A., Nicholson P.D., Stephan K., Jaumann R., Sotin C., Baines K.H., *et al*. 2012. Modeling specular reflections from hydrocarbon lakes on titan. Icarus 220:744–751.

Sotin C., Barnes J.W., Lawrence K.J., Soderblom J.M., Audi E., Brown R.H., Le Mouelic S., Baines K.H., Buratti B.J., Clark R.N., *et al*. 2015. Tidal currents between titan's seas detected by solar glints. AGUFM 2015:P12B–04.

Sotin C., Lawrence K., Reinhardt B., Barnes J., Brown R.H., Hayes A., Le Mouélic S., Rodriguez S., Soderblom J., Soderblom L., *et al*. 2012. Observations of titan's northern lakes at 5 μm: Implications for the organic cycle and geology. Icarus 221:768–786.

Steckloff J.K., Soderblom J.M., Farnsworth K.K., Chevrier V.F., Hanley J., Soto A., Groven J.J., Grundy W.M., Pearce L.A., Tegler S.C., *et al*. 2020. Stratification dynamics of titan's lakes via methane evaporation. The planetary science journal 1:26.

Stephan K., Jaumann R., Brown R.H., Soderblom J.M., Soderblom L.A., Barnes J.W., Sotin C., Griffith C.A., Kirk R.L., Baines K.H., *et al*. 2010. Specular reflection on titan: liquids in kraken mare. Geophysical Research Letters 37.

Stofan E.R., Elachi C., Lunine J.I., Lorenz R.D., Stiles B., Mitchell K., Ostro S., Soderblom L., Wood C., Zebker H., *et al*. 2007. The lakes of titan. nature 445:61–64.

Strong A.E. and Ruff I.S. 1970. Utilizing satellite-observed solar reflections from the sea surface as an indicator of surface wind speeds. Remote sensing of environment 1:181–185.

Toffoli A. and Bitner-Gregersen E.M. 2017. Types of ocean surface waves, wave classification. Encyclopedia of Maritime and Offshore Engineering pages 1–8.

Tokano T. 2009. Impact of seas/lakes on polar meteorology of titan: Simulation by a coupled gcm-sea model. Icarus 204:619–636.

Tokano T. 2010. Simulation of tides in hydrocarbon lakes on saturn's moon titan. Ocean dynamics 60:803–817.

Tokano T. and Lorenz R.D. 2015. Wind-driven circulation in titan's seas. Journal of Geophysical Research: Planets 120:20–33.

Tokano T. and Lorenz R.D. 2016. Sun-stirred kraken mare: Circulation in titan's seas induced by solar heating and methane precipitation. Icarus 270:67–84.

Tokano T., Lorenz R.D., and Van Hoolst T. 2014. Numerical simulation of tides and oceanic angular momentum of titan's hydrocarbon seas. Icarus 242:188–201.

Tomasko M., Doose L., Engel S., Dafoe L., West R., Lemmon M., Karkoschka E., and See C. 2008. A model of titan's aerosols based on measurements made inside the atmosphere. Planetary and Space Science 56:669–707.

Turtle E., Perry J., Barbara J., Del Genio A., Rodriguez S., Le Mouélic S., Sotin C., Lora J., Faulk S., Corlies P., *et al*. 2018. Titan's meteorology over the cassini mission: Evidence for extensive subsurface methane reservoirs. Geophysical Research Letters 45:5320–5328.

Vincent D., Karatekin Ö., Lambrechts J., Lorenz R.D., Dehant V., and Deleersnijder É. 2018. A numerical study of tides in titan s northern seas, kraken and ligeia maria. Icarus 310:105–126.

Vixie G., Barnes J.W., Jackson B., Rodriguez S., Le Mouélic S., Sotin C., MacKenzie S., and Wilson P. 2015. Possible temperate lakes on titan. Icarus 257:313–323.

Wall S., Hayes A., Bristow C., Lorenz R., Stofan E., Lunine J., Le Gall A., Janssen M., Lopes R., Wye L., *et al*. 2010. Active shoreline of ontario lacus, titan: A morphological study of the lake and its surroundings. Geophysical Research Letters 37.

Wasiak F., Androes D., Blackburn D., Tullis J., Dixon J., and Chevrier V. 2013. A geological characterization of ligeia mare in the northern polar region of titan. Planetary and Space Science 84:141–147.

Wolanski E., Ridd P., and Inoue M. 1988. Currents through torres strait. Journal of Physical Oceanography 18:1535–1545.

Wye L., Zebker H., and Lorenz R. 2009. Smoothness of titan's ontario lacus: Constraints from cassini radar specular reflection data. Geophysical Research Letters 36.

Young I. 1999. Seasonal variability of the global ocean wind and wave climate. International Journal of Climatology: A Journal of the Royal Meteorological Society 19:931–950.

Zebker H., Hayes A., Janssen M., Le Gall A., Lorenz R., and Wye L. 2014. Surface of ligeia mare, titan, from cassini altimeter and radiometer analysis. Geophysical Research Letters 41:308–313.

Zebker H.A., Stiles B., Hensley S., Lorenz R., Kirk R.L., and Lunine J. 2009. Size and shape of saturn's moon titan. Science 324:921–923.